Development of a nuclear quadrupole based technique for measuring charge homogeneity, and its application for YBCO

SHAHAR LEVY

DEVELOPMENT OF A NUCLEAR QUADRUPOLE BASED TECHNIQUE FOR MEASURING CHARGE HOMOGENEITY, AND ITS APPLICATION FOR YBCO

RESEARCH THESIS

SUBMITTED IN PARTIAL FULFILLMENT OF THE REQUIREMENTS
FOR THE DEGREE OF MASTER OF SCIENCE
IN PHYSICS

SHAHAR LEVY

SUBMITTED TO THE SENATE OF THE TECHNION
ISRAEL INSTITUTE OF TECHNOLOGY
Syvan, 5763 Haifa June 2003

The research thesis was done under the supervision of Prof. Amit Keren in the faculty of physics.

I am deeply grateful to Amit Keren for his excellent guidance, his support and encouragement throughout this long period, and for his efforts to inspire me with self-confidence and to impart me with experience for my future endeavors.

I thank Prof. Emil Polturak for his extensive support throughout my research work. For encouraging me in his special way, and for teaching me what real experimental physics is.

A thank you from the bottom of my heart goes to the lab technicians- Galina Bazalitzky, Mordechai Ayalon, Shmuel Hoida and Dr. Leonid Iomin for all their help, which was always given gladly.

Thanks to all my friends in the research group of magnetism and superconductivity- Eva, Rinat, Oren, Oshri, Ariel, Lior and Meni for the wonderful working atmosphere they created.

And last but not least- a warm thank you to Amit Kanigel for his ample help with professional issues, and for his support in the personal domain.

The generous financial help of the Technion is gratefully acknowledged.

To my parents, Dvora and Nahum, for their infinite love and support

Contents

Abstract **1**

List of symbols and abbreviations **3**

1. Introduction **4**

2. Main Results **10**
   - 2.1. Theory…….. 10
   - 2.2. Orientation……... 12
   - 2.3. Frequency sweep……. 12
   - 2.4. ADNQR experimental results…….. 14

3. Main Conclusions **16**

4. NQR **17**
   - 4.1. Quadrupole interaction – classical approach…….. 17
   - 4.2. Quantum mechanical formalism…….. 19
     - 4.2.1. Interaction with an external time dependent magnetic field…… 22
   - 4.3. Magnetization after a spin echo sequence…….. 27
   - 4.4. Summary……. 30

5. YBCO – Structure and properties **32**

6. Sample Preparation and Characterization **36**
   - 6.1. Preparation…….. 36
   - 6.2. Characterization method, x-ray diffraction…… 37
     - 6.2.1. Practical considerations for the x-ray experiment…….. 41
   - 6.3. Summary……. 41

7. Fit to data **42**
   - 7.1. Broadening effects…… 42
   - 7.2. Orientation of the EFG tensor…….. 44
     - 7.2.1. Correction of the equation……... 45

8. Advantages and Disadvantages **47**

A Spin ½ in magnetic field **49**

B A Special case of NQR - η=0 **57**

C Experimental Aspects of NMR/NQR **66**

Bibliography **80**

List of Figures

1.1 T_C/ T_C^{max} and T_g/ T_C^{max} vs. $\Delta p_m = p_m - p_m^{max}$. T_C^{max} is the maximum T_C achievable 5
1.2 The electric quadrupole interaction gives different energies for different orientation of the nucleus (ellipse)…… 6
1.3 Basic ADNQR configuration. A sample (circle) with a preferred direction (marked by a line) is inserted into a coil. The angle between them, θ , can be varied…….…….. 8
1.4 The samples have cylindrical shape. The alignment direction (z) is marked by a line…… 9
2.1 Intensity vs. θ for different values of η in an ADNQR experiment. Theoretical result…… 11
2.2 Intensity ratio, $<M_{coil}>(0,\eta)/<M_{coil}>(90,\eta)$ vs. η. Theoretical result…….. 12
2.3 The NQR spectrum of our samples at 100K…….. 13
2.4 ADNQR experimental result for $YBCO_7$ at 31.15MHz…….. 14
2.5 ADNQR experimental result for $YBCO_{6.675}$ at 27.501MHz, and $YBCO_7$ at 30.53MHz (shoulder). The result for the main peak of $YBCO_7$ is the same one that appears in Fig 2-4…… 15
4.1 The Wigner-Eckhart theorem connects the coordinate representation to the angular momentum representation by a constant…… 21
4.2 Schematic description of a spin echo sequence. Two pulses, π/2 and π, separated by a pause of time τ. For more details see appendix C…..…… 27
4.3 The echo intensity, for θ=π/2, as a function of the pulse length. The optimal value, $t_{\pi/2}$, was determined from the first maximum, and is independent of η. 31
5.1 YBCO structure and notation……. 33
5.2 Lattice parameters of YBCO vs. oxygenation at room temperature. [10]……..…. 34
5.3 Phase diagram of YBCO……. 35
6.1 Interference by reflection from two parallel planes. When the optical length difference - 2dsinθ, is equal to a multiple of the wave length we obtain the Bragg formula……. 37
6.2 x-ray result of the $YBCO_7$ samples. Those samples were prepared by shaking. Lower graph, disoriented sample. Upper and middle, oriented sample……. 38
6.3 Each tiny grain of the powder is a single crystal, represented in this figure as 9 joined unit cells. The (001) planes are marked in gray, and are all parallel throughout the all sample. This plane direction is marked by a line on the sample, as illustrated in the right cylinder…… 39
6.4 x-ray result for the $YBCO_7$ sample. This sample was prepared without shaking 40
6.5 x-ray result for the $YBCO_{6.675}$ sample. This samples was prepared without shaking…… 40
7.1 Theoretical and experimental results for the peak of $YBCO_7$. The line represents the best fit, including the broadening effect (see text). The fit results are η=0±0.1 and σ=15°. The RF frequency is 31.15MHz…… 43
7.2 Theoretical and experimental results for the shoulder of $YBCO_7$. The line represents the best fit, including the broadening effect (see text). The fit results are η=0.6±0.1 and σ=15°. The RF frequency is 30.53MHz……..…… 44
7.3 Theoretical and experimental results for $YBCO_{6.675}$. The line represents the best fit, including the broadening effect with the same width as for the $YBCO_7$ case

(see text). The fit result is η=1. The RF frequency is 27.501MHz……. 45
7.4 The coil orientation for different EFG orientations. Left: Vzz ‖ c (as in Cu(2) of $YBCO_7$. Right: Vzz ‖ a (as in Cu(1) of $YBCO_7$)……. 46
A.1 Magnetic fields configuration in a basic NMR experiment. The coil produces a time dependent field - $2B_1$, perpendicular to a strong static field B_0……. 51
A.2 The π/2 pulse rotates the spin from the z direction to y'. During the pulse time the frame S' rotates with angular velocity ω_0 around the z axis……. 55
B.1 Spin evolution for the up and down subspaces during the π/2 pulse……. 65
B.2 Spin evolution for the up and down subspaces after the π/2pulse……. 65
C.1 Block diagram for NQR system……. 67
C.2 Schematic description of a duplexer circuit…… 69
C.3 The equivalent duplexer circuit during the RF pulse…….. 69
C.4 The equivalent duplexer circuit after the RF pulse……. 70
C.5 The NMR/NQR probe……... 71
C.6 Schematic description of a Spin Echo sequence. Two pulses followed by a gaussian shape echo…… 73
C.7 A schematic pulse sequence for measuring T_1……... 79

Abstract

The phenomenon of high temperature superconductivity (HTSC) has focused a huge research effort for the last two decades. Yet the mechanism for HTSC is not clear yet. The experimental evidence points to the fact that the CuO_2 planes play a major role in this mechanism, therefore much of the theoretical work concentrates on the contribution of those planes to superconductivity. One of the dominant theories bases the superconductivity mechanism on the creation of charge stripes in those planes (the stripes theory). The theory is supported by experimental results, obtained first by neutron scattering, and latter supported by many other techniques, like NQR, STM and μSR, and their existence is no longer doubted. The important question is whether they are crucial for the mechanism of superconductivity.

Other techniques differ from the theory of stripes in that they don't take the inhomogeneity inside the planes to be involved in the mechanism of HTSC. A way to check the validity of those theories is by measuring T_c, the superconductivity phase transition temperature, as a function of the charge inhomogeneity in the planes. The dependence of T_c on doping is known experimentally. Therefore, by measuring the inhomogeneity as a function of doping we can achieve important information regarding the relation between T_c and homogeneity.

However, there are some experimental problems. With all those techniques we've mentioned it is still difficult (if possible) to obtain data on the inhomogeneity level in the planes for the entire doping range. We chose to attack the problem with a new NQR technique we developed especially for this purpose. We prove, experimentally and theoretically, that this method can addresses the above question.

This work deals with two aspects. Firstly is the development of the new technique, which we call angle dependent NQR (ADNQR), and checking experimentally that the method indeed works for known cases. Secondly, we applied the technique for $YBCO$, a type of high temperature superconductor, and measured the dependence of the charge inhomogeneity on doping. **We found that as doping increases inhomogeneity decreases, namely, there is anti correlation between** T_c and homogeneity. This result contradicts the importance of stripes

for high temperature superconductivity.

List of Symbols and Abbreviations

Symbol	Meaning
NQR	Nuclear Quadrupole Resonance
NMR	Nuclear Magnetic Resonance
ADNQR	Angle Dependent NQR
EFG	Electric Field Gradient
η	Asymmetry parameter
Q	Quadrupole moment of a nucleus
$V_{\alpha\beta}$	The EFG tensor
B_0	Static homogenous magnetic field in the z direction
B_1	RF magnetic field
$\hat{H}$	Hamiltonian
$\hat{H}_q$	Pure quadrupole Hamiltonian
$\hat{H}_0$	Spin $\frac{1}{2}$ Hamiltonian in a magnetic field B_0
$Cu(1), Cu(2)$	Chain and Planes copper in YBCO respectively
a, b, c	YBCO lattice constants
γ	Gyromagnetic ratio
$\hat{\mathbf{I}}$	Angular momentum operators
$\hbar$	Planck's constant
Ψ, φ	Wave functions
t	Time
$t_{\frac{\pi}{2}}, t_\pi$	Length of $\frac{\pi}{2}$ and π pulses respectively
τ	Break time between pulses in a spin echo sequence
$\hat{U}_0^{NMR}(t), \hat{U}_0^{NQR}(t)$	Time propagator for $\hat{H}_0$ and $\hat{H}_q$ respectively
$\hat{U}_{pulse}^{NMR}(t)$	Time propagator for $\hat{H}_0$ during RF pulse in the x direction
$\hat{U}_{pulse}(t)$	Time propagator for $\hat{H}_q$ during RF
$\hat{U}_{pulse}^{\eta=0}(t)$	Time propagator for $\hat{H}_q$ during RF pulse in the x direction for $\eta = 0$

Chapter 1

Introduction

The mechanism for superconductivity in the cuprates is perhaps the most challenging question in solid state physics today, and draws the attention of literally thousands of researchers. The presence of CuO_2 planes in the structure of all cuprates leads these researchers to believe that a single theory could explain superconductivity in all of them. One of the main focal theories is based on the presence of stripes, discovered in $La_{2-x}Sr_xCu_1O_4$ [20], and suggested to be a critical feature for superconductivity by Emery and Kivelson [2]. The concept of stripes is based on the fact that in the CuO_2 plane the valence of the Cu could be Cu^{+2} with a spin 1/2 or Cu^{+3} with no spin. The number of Cu^{+3} per CuO_2 is referred to as the doping level p_m. For stripes to occur the Cu^{+2} ions must phase separately from the Cu^{+3} ions, and both phases should be one dimensional. Indeed, it is now established by many different experiments sensitive to internal magnetic fields that at low doping most of the cuprates phase separately into "hole rich" and "hole poor" regions. The supporting evidence for this separation (in the bulk) is that when under-doped cuprates are cooled down, they first start to superconduct at T_c, and then, upon further cooling, develop a static magnetic field characteristic of spin glass (random orientation) at a temperature T_g. This finding seems to support the importance of stripes for superconductivity. However, the indications for phase separation disappear as doping increases, namely $T_g(p_m) \rightarrow 0$ as p_m increases. This can be seen in the combined phase diagram of many superconductors presented in Fig 1-1. This figure depicts both $T_c/T_c^{\max}$ and $T_g/T_c^{\max}$ vs. $\Delta p_m = p_m - p_m^{\max}$ where $T_c^{\max}$ is the maximum T_c achievable by doping a certain compound, and $p_m^{\max} \sim 0.16$ is the optimum doping level. From this figure it is clear that there

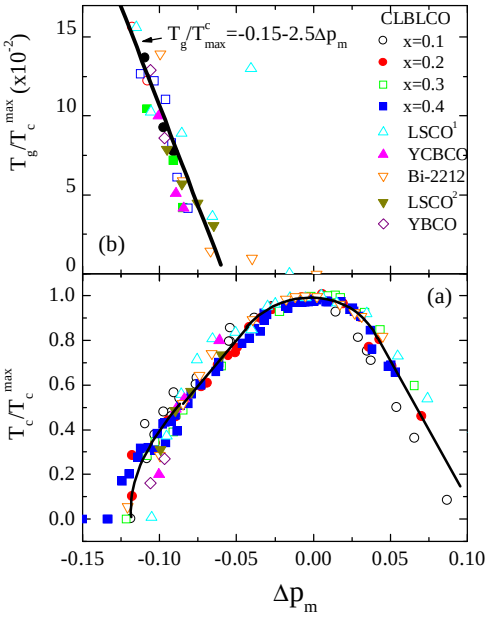

Figure 1-1: $T_c/T_c^{\max}$ and $T_g/T_c^{\max}$ vs. $\Delta p_m = p_m - p_m^{\max}$. $T_c^{\max}$ is the maximum T_c achievable.

is no "magnetic" evidence for phase separation in doping higher than $\Delta p_m = -0.05$ ($p_m > 0.11$) and certainly not in optimally doped cuprates. Therefore one might jump to the conclusion that phase separation is not important for superconductivity since it is not always present.

However, the lack of spontaneous magnetic fields does not rule out phase separation. It could simply mean that the "hole poor" regions are far away from each other, and/or their interaction is screened by the superconducting "hole rich" regions. Thus their freezing temperature could simply not be experimentally accessible. In order to prove or disprove phase separation in optimally doped samples one must perform an experiment that is sensitive to the charge fluctuations on the CuO_2 plane. If *each* Cu atom turns out to "see" the same charge distribution around it, then no phase separation is possible. The ideal technique to meet this challenge is Nuclear Quadrupole Resonance (NQR).

Standard NQR is based on the fact that the Cu nuclei with their spin $I = 3/2$ could be viewed as oval objects positively charged; see ellipse in Fig 1-2. As a result, their energy inside a solid depends on their orientation. When the nuclei poles are close to positive charges their

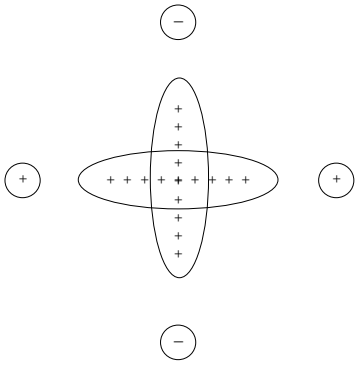

Figure 1-2: The electric quadrupole interaction gives different energies to different orientation of the nucleus (ellipse).

energy is high. However, when the poles are close to the negative charges the energy is low. The energy difference between one orientation to the next is determined by the Electric Field Gradient (EFG), namely, the second derivative of the electrostatic potential $V(\mathbf{r})$ at the position of the Cu nuclei. V, in turn, depends on the surrounding charges. When all three dimensions are considered, the NQR Hamiltonian is given by

$$\hat{H}_q = \frac{\hbar\omega_0}{6}\left[3\hat{I}_z^2 - \hat{\mathbf{I}}^2 + \eta\left(\hat{I}_x^2 - \hat{I}_y^2\right)\right]. \tag{1.1}$$

A full derivation of this Hamiltonian will be given in chapter 4. Here we only mention that ω_0 is a frequency scale determined by the EFG $V_{zz} = \frac{\partial^2 V}{\partial z^2}$. For copper atoms in the CuO_2 planes of $YBCO$, z is the direction perpendicular to these planes. Since we have no model for V there is very little information we can draw from ω_0. On the other hand

$$\eta \triangleq \frac{V_{xx} - V_{yy}}{V_{zz}}$$

where in our case x and y are directions in the CuO_2 plane. The important point is that η is a dimensionless number in the range $[-1, 1]$ (in our notation), which measures charge and crystal symmetry. If $\eta = 0$ then the planes are symmetric under the interchange of the x and y directions.

The technical aspects of NQR are described in details in appendix C, and the theory in

chapter 4. Here we only mention that the NQR signal is detected by power transmission in two pulses, of duration $t_{\pi/2}$ and $2t_{\pi/2}$, to a coil at a Radio Frequency (RF) f. This power creates a field $2B_1$ in the direction of the coil, and adds a time dependent perturbation term to the Hamiltonian (during the pulses) of the form

$$\hat{W} = 2\omega_1 \cdot \widehat{\mathbf{n}} \cos(2\pi f t)$$

where $\omega_1 = {}^{63}\gamma \mathbf{B}_1$, ${}^{63}\gamma$ is the ^{63}Cu gyromagnetic ratio, and

$$\widehat{\mathbf{n}} = (\sin\theta\cos\phi, \sin\theta\sin\phi, \cos\theta)$$

is some direction in the reference frame set by the crystal directions. f is swept until it matches an energy difference between two eigenstates of the Hamiltonian given in Eq 1.1. When this resonance condition is met an echo is formed in the coil. This echo is an induced oscillatory voltage in the coil, at the frequency f (without any external transmission of power).

The energy levels of the NQR Hamiltonian for the spin 3/2 Cu are two doublets so that there is only one resonance frequency, which, as we show in chapter 4 is given by

$$f = \frac{\omega_0}{2\pi}\sqrt{1+\frac{\eta^2}{3}}$$

Therefore ω_0 and η could not be separately determined from f. Up to date, η was determined with the help of a Nuclear Magnetic Resonance (NMR) experiment by applying a strong external static magnetic field (${}^{63}\gamma H \gg \omega_0$). This led to three resonance frequencies, each one depends linearly on η, out of which η could be extracted. The drawback of this approach is that the average resonance frequency is determined by the averaged η, which could be zero even if locally it is not. In other words, NMR can not provide direct information on η fluctuations. In order to overcome this difficulty we developed a new experimental strategy which we call Angle Dependent NQR (ADNQR).

In ADNQR the measured signal intensity is proportional to the nuclear magnetization in the direction of the coil at the echo $\left\langle \mathbf{M}^{coil} \right\rangle (\theta, \eta)$, and it is a function of the orientation of the coil with respect to the crystal $\widehat{z}$ directions. This is shown in Fig 1-3. The $\langle\rangle$ brackets stand

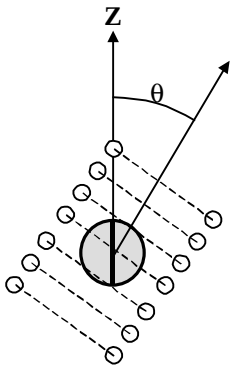

Figure 1-3: Basic ADNQR configuration. A sample (circle) with a preferred direction (marked by a line) is inserted into a coil. The mutual angle between them, θ, can be varied.

for thermal average. In chapter 4 we develope the theory for this experiment and show, in particular, that $\left\langle \mathbf{M}^{coil} \right\rangle (\theta, \eta)$ is a measure of $|\eta|$. Therefore, the sample average of $\left\langle \mathbf{M}^{coil} \right\rangle (\theta, \eta)$ is not determined by the averaged η. In other words, if η is distributed around zero it will still contribute to $\left\langle \mathbf{M}^{coil} \right\rangle (\theta, \eta)$. Thus the ADNQR method allows us to measure the fluctuations in η. When stripes, or any other kind of phase separation, exists one would expect strong η fluctuations.

We apply the ADNQR experiment to $YBa_2Cu_3O_y$ $[YBCO_y]$. A review on the crystal and superconducting properties of this compound is given in chapter 5. In short, in the doping levels relevant to us this system is orthorhombic ($b > a$), and the ratio b/a grows as doping increases. Two out of the three Cu in the unit formula reside in the CuO_2 planes, and one in the chains. There are also two isotopes so four resonance lines altogether. In addition, the NQR frequency depends on doping. Thus, the first experiment we performed was a sites assignment (frequency sweep) which is described in section 2.3. Once we determined the resonance frequency for each Cu we started with the ADNQR.

We chose to work with $YBCO$ since this compound is perhaps the best for NQR; it has the narrowest resonance lines. On the other hand, there are no single crystals of $YBCO$ and we worked with powders which were oriented in a 8 T magnetic field and glued with staycast. After the orientation the sample has a cylindrical shape as depicted in Fig 1-4. The orientation procedure ensures that the $\widehat{z}$ direction (marked with a line) of most powder grains points in

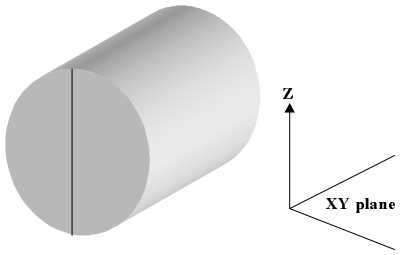

Figure 1-4: The samples have cylinderical shape. The alignment direction (z) is marked by a line.

the direction of the external field. However the $\widehat{x}$ and $\widehat{y}$ directions are mixed. The orientation procedure and its x-ray tests are described in chapter 6. We examine y values which are at optimum ($y = 7.0$) and at the highest doping on the $T_c = 60$ K plateau ($y = 6.675$). These are out of the range where T_g is detectable, and our ADNQR indeed yields new information of the local charge fluctuation evolution with doping of $YBCO$.

Chapter 2

Main Results

2.1 Theory

In chapter 4 we show that in a single crystal the magnetization in the coil at the time of the echo is given by

$$\left\langle \mathbf{M}^{coil} \right\rangle (\theta, \phi, \eta) = N \frac{f}{2k_B T} \epsilon \sin^3(2\epsilon\omega_1 t_{\frac{\pi}{2}}) \tag{2.1}$$

where θ and ϕ are the direction angles of the coil with respect to the crystal directions and both the thermal population factor f/k_BT and ω_1 are multiplied by an efficiency factor

$$\epsilon = \sqrt{\left[a_x^2 \cos^2(\phi) + a_y^2 \sin^2(\phi)\right] \sin^2(\theta) + a_z^2 \cos^2(\theta)}, \tag{2.2}$$

where

$$\mathbf{a} = \frac{1}{2\sqrt{3+\eta^2}} (\eta + 3, \eta - 3, 2\eta) .$$

Equation 2.1 is our main theoretical achievement. For $\eta = 0$, $\theta = 90$, ϵ is reduced to $\sqrt{3}/2$, a result first obtained by Das and Hahn [7]. In our situation we must average on ϕ and obtain

$$\left\langle \mathbf{M}^{coil} \right\rangle (\theta, \eta) = \frac{Nf}{2k_B T} \int_0^{2\pi} d\phi \epsilon \sin^3(2\epsilon\omega_1 t_{\frac{\pi}{2}}) \tag{2.3}$$

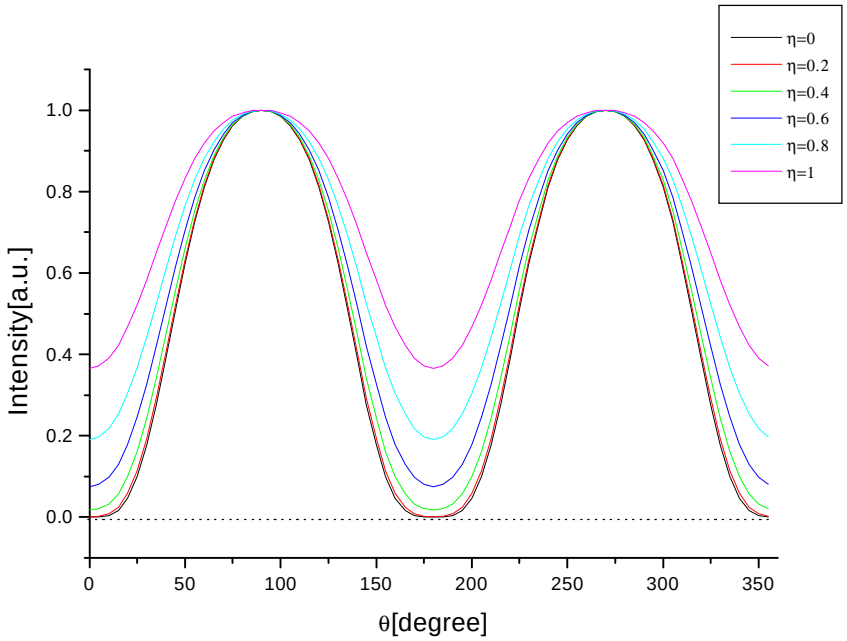

Figure 2-1: Intensity vs. θ for different values of η in an ADNQR experiment.

This averaging must be done numerically and yields the result presented in Fig 2-1. This graph shows an explicit dependence of the echo intensity on the value of η. The most dominant difference that η creates is to change the intensity ratio of $\theta = 0$ (180, 360) and $\theta = 90$ (270). Fig 2-2 shows the predicted ratio as a function of η from the numerical calculation. As mentioned before, the result does not depend on the sign of η. In fact, for small η one can show that.

$$\frac{\langle \mathbf{M}^{coil} \rangle (0, \eta)}{\langle \mathbf{M}^{coil} \rangle (90, \eta)} = \frac{2\pi^3}{81}\eta^4 + O(\eta^6).$$

In a real crystal there will be η fluctuations. However positive and negative η values will equally contribute to the ratio $\langle \mathbf{M}^{coil} \rangle (0, \eta) / \langle \mathbf{M}^{coil} \rangle (90, \eta)$. If this ratio is small it means that all η's are small.

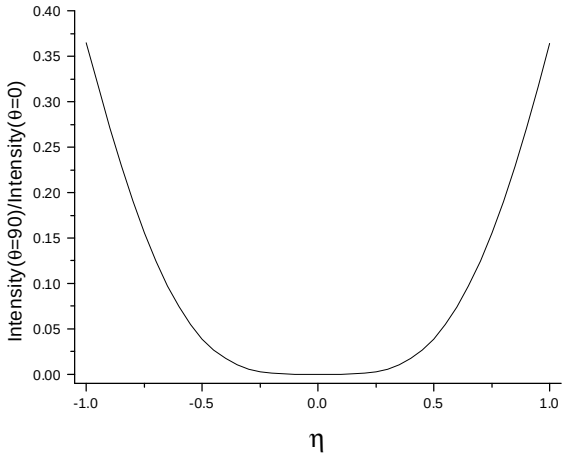

Figure 2-2: Intensity ratio, $\langle \mathbf{M}^{coil} \rangle (0, \eta) \,/\, \langle \mathbf{M}^{coil} \rangle (90, \eta)$, vs η. Theoretical result.

2.2 Orientation

We demonstrate using x ray (see chapter 6) that our orientation procedure is efficient in aligning the powder grains. However, the x-ray test is done only on the surface of the sample shown in Fig 1-4, and it is therefore hard to know qualitatively what is the true orientation quality of the bulk. Nevertheless, it is clear that the orientation of the $YBCO_{6.675}$ is better than that of $YBCO_7$. This result is reasonable since the sample with lower doping is more magnetic. For our conclusions this fact is sufficient.

2.3 Frequency sweep

In Fig 2-3 we show the lines at 100K. At room temperature we found the following lines: The resonance frequency of the in plane ^{63}Cu/^{65}Cu in $YBCO_7$ [$Cu_7(2)$] is 31.15/29.3 MHz. The line is reasonably narrow with a width of 0.5 MHz. There is a low frequency shoulder at about 30.5 MHz which is probably due to not perfectly doped grains. The resonance of the in plane ^{63}Cu in $YBCO_{6.675}$ [$Cu_{6.675}(2)$] is at 27.2 MHz. Its width is 1.5 MHz. Finally, the chain ^{63}Cu in $YBCO_{6.675}$ [$Cu_{6.675}(1)$] is located at 30 MHz.

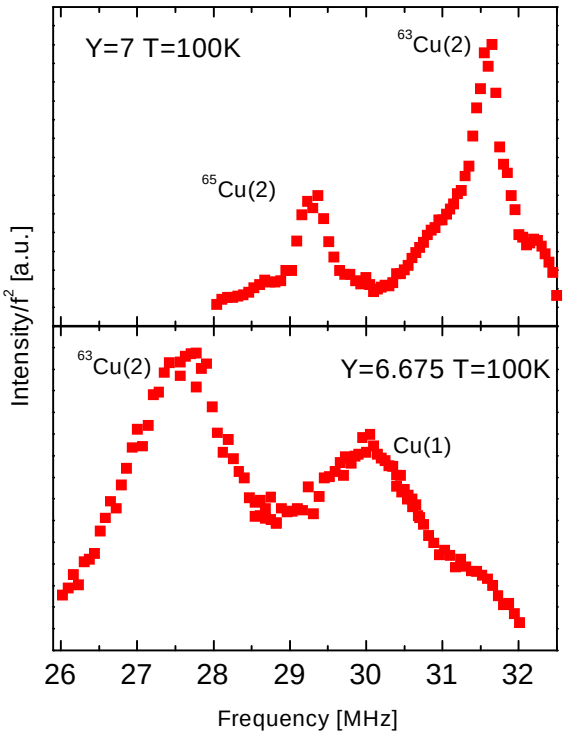

Figure 2-3: The NQR spectrum of our samples at 100K.

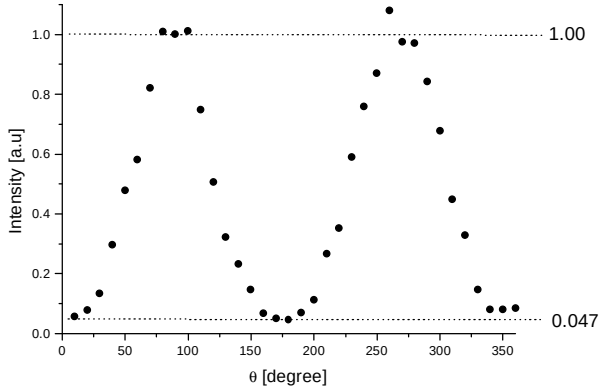

Figure 2-4: ADNQR experimental result for $YBCO_7$ at 31.15MHz.

2.4 ADNQR experimental results

In Fig 2-4 we present the experimental results for $YBCO_7$. In this case we changed the angle over 360 degrees. And, indeed, as the theory predicts, the signal intensity depends periodically on θ. In addition, the intensity at $\theta = 0$ (and 180 and 360) is lower by a factor of 20 than at $\theta = 90$ (and 270). From the ratio $\left\langle \mathbf{M}^{coil} \right\rangle (0, \eta) \,/\, \left\langle \mathbf{M}^{coil} \right\rangle (90, \eta) = 0.05$ one can conclude that $\eta = 0.5$ if the $YBCO_7$ is perfectly oriented.

In Fig 2-5 we depict the main experimental achievement of this thesis, namely, the ADNQR results of both $YBCO_7$ and $YBCO_{6.675}$. Again, the results for $YBCO_{6.675}$ fit the general behavior of our prediction -the intensity at $\theta = 0$ is 60% lower than at $\theta = 90$. However, according to our theoretical calculations (Fig 2-1) the intensity at $\theta = 0$ can not exceed 40% of the intensity at $\theta = 90$. The main reason for this discrepancy is not clear yet. Nevertheless, it is consistent with larger η for $YBCO_{6.675}$. In fact, it seems from the increasing intensity on the shoulder with respect to the intensity on the peak that η continuously increases with decreasing doping. The significance of this figure is discussed in the next section: main conclusions.

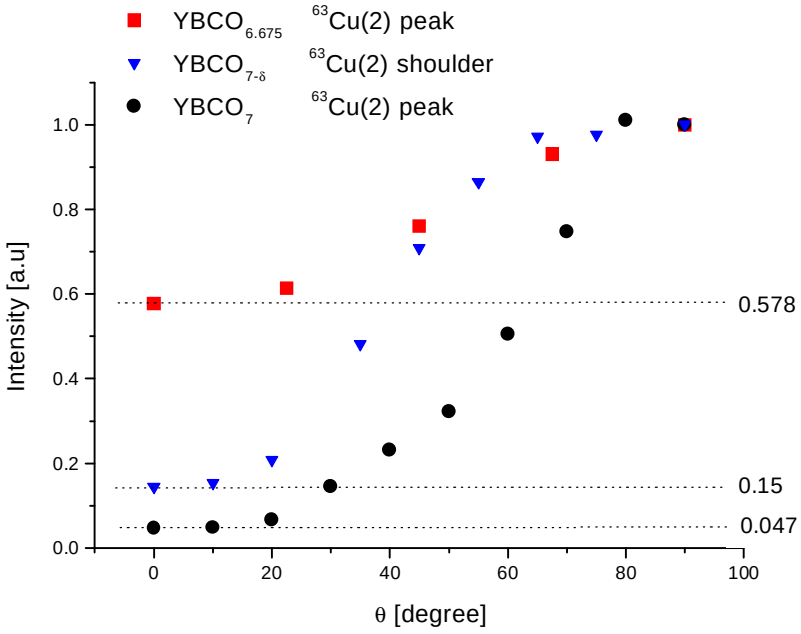

Figure 2-5: ADNQR experimental result for $YBCO_{6675}$ at 27.501MHz and $YBCO_7$ at 30.53MHz (shoulder). The result for the main peak of$YBCO_7$ is the same one that appears in Fig 2-4.

Chapter 3

Main Conclusions

1. ADNQR can be applied successfully to measure η, and η fluctuations.

2. Despite the fact that $YBCO_7$ is less oriented than $YBCO_{6.675}$, and that it has a less symmetric crystal structure, our data is consistent with $YBCO_7$ having the smaller values of $|\eta|$. If we consider the η fluctuations in $YBCO_7$ to be minimal, our experiment means that there must be stronger charge inhomogeneities in $YBCO_{6.675}$ in order to explain its larger $|\eta|$ values. This is the first evidence for charge inhomogeneities in such highly doped YBCO.

3. Because of the failure of our theory to explain the absolute result of η in $YBCO_{6.675}$ we avoid making conclusions at this point regarding the absolute value of η in $YBCO_7$. It is conceivable that the lack of perfect orientation or non uniformity of the RF field inside the coil contributes to this failure. Nevertheless, we can safely say that as doping increases, charge homogeneity increases, and this occurs all the way to optimum doping.

4. Conclusion 2 seems to contradict the importance of stripes for high T_c. However, to be on the safe side, one must carefully measure η as a function of doping and see if it saturates at some doping level, or decreases continuously as doping increases.

5. The fact that the ADNQR result of $YBCO_{6.675}$ doesn't fully fit the calculated prediction urged us to search for other effects we didn't take into account. This is done in chapter 7.

Chapter 4

NQR

4.1 Quadrupole interaction-classical approach

Quadrupole energy

In the case of a spin $\frac{1}{2}$ in a magnetic field (appendix A) the energy levels of the system are due to magnetic interactions with the external magnetic field $\mathbf{B_0}$. In the NQR case the energy mechanism originates in the electric interaction of the nucleus's charge with the electric potential, namely

$$E = \int \rho(\mathbf{r}) V(\mathbf{r}) d\mathbf{r} \tag{4.1}$$

Where $\rho(\mathbf{r})$ is the charge density of the nucleus and $V(\mathbf{r})$ is the electric potential in its vicinity.

We choose the nucleus center of mass as the origin and expand $V(\mathbf{r})$ in a Taylor's series to get

$$V(\mathbf{r}) = V(0) + \sum_{\alpha} \mathbf{r}_\alpha \left(\frac{\partial V}{\partial \mathbf{r}_\alpha} \right)_{\mathbf{r}=\mathbf{0}} + \frac{1}{2} \sum_{\alpha\beta} \mathbf{r}_\alpha \mathbf{r}_\beta \left(\frac{\partial^2 V}{\partial \mathbf{r}_\alpha \partial \mathbf{r}_\beta} \right)_{\mathbf{r}=\mathbf{0}} + ... \tag{4.2}$$

Substituting 4.2 into 4.1 yields then

$$E = V(0) \int \rho(\mathbf{r}) d\mathbf{r} + \sum_{\alpha} V_\alpha \int \mathbf{r}_\alpha \rho(\mathbf{r}) d\mathbf{r} + \frac{1}{2} \sum_{\alpha\beta} V_{\alpha\beta} \int \mathbf{r}_\alpha \mathbf{r}_\beta \rho(\mathbf{r}) d\mathbf{r} + .. \tag{4.3}$$

Where $V_\alpha \triangleq \left(\frac{\partial V}{\partial \mathbf{r}_\alpha}\right)_{\mathbf{r}=\mathbf{0}}$, $V_{\alpha\beta} \triangleq \left(\frac{\partial^2 V}{\partial \mathbf{r}_\alpha \partial \mathbf{r}_\beta}\right)_{\mathbf{r}=\mathbf{0}}$ and $\alpha, \beta = x, y, z$. $V_{\alpha\beta}$ is the so called electric field gradient (EFG) tensor.

The first term of Eq 4.3 is the electric monopole, it gives the electrostatic energy of the nucleus. The second term involves the interaction of the nucleus with the electric field through its electric moment. In the center of mass frame the electric dipole moment vanishes, thus leading us to treat the third term, the quadrupole interaction.

The EFG tensor

In this interaction the environment is taken into account by the EFG, and it expresses the spatial change of the electric field in the vicinity of the nucleus. This change is due to asymmetry in the nucleus environment. For instance, a vacancy in a perfect crystal causes an EFG around it. Like in the spin $\frac{1}{2}$ case, where the external magnetic field has defined a clear direction in space (z), we can use in this case the EFG tensor to define a reference frame in space. We do so by taking the diagonal form of the EFG tensor

$$V = \begin{pmatrix} V_{xx} & 0 & 0 \\ 0 & V_{yy} & 0 \\ 0 & 0 & V_{zz} \end{pmatrix} \tag{4.4}$$

and the three directions are defined by

$$|V_{xx}| \leq |V_{yy}| \leq |V_{zz}| \tag{4.5}$$

By assuming that the electric field at the nucleus is produced entirely by charges wholly external to the nucleus we can use Laplace's equation $V_{xx} + V_{yy} + V_{zz} = 0$ and reduce the number of parameters of the EFG so that

$$V = eq \begin{pmatrix} -\frac{1-\eta}{2} & 0 & 0 \\ 0 & -\frac{1+\eta}{2} & 0 \\ 0 & 0 & 1 \end{pmatrix} \tag{4.6}$$

with

$$eq \triangleq V_{zz} \tag{4.7}$$

$$\eta \triangleq \frac{V_{xx} - V_{yy}}{V_{zz}} \Rightarrow \quad -1 \leq \eta \leq 0 \tag{4.8}$$

We emphasize here that the importance of the EFG tensor is in reflecting the symmetry of the nucleus's environment.

The quadrupole tensor

All the intrinsic properties of the nucleus himself, which are relevant for the quadrupole interaction, are included in the term

$$Q_{\alpha\beta} = \int \left[3\mathbf{r}_\alpha \mathbf{r}_\beta - \delta_{\alpha\beta}\mathbf{r}^2\right] \rho(\mathbf{r}) d\mathbf{r} \tag{4.9}$$

This term is included in the third term of the RHS of Eq 4.3, in a slightly different form that changes nothing but adds a constant shift in the energy levels. By changing the orientation of the nucleus with respect to the EFG reference frame (see Fig 1-2) we change the quantity $\rho(\mathbf{r})$ of the tensor and by doing so we might change the energy levels of the nucleus.

Using 4.9 and 4.6 in 4.3 we can write the quadrupole energy as

$$E_{quadrupole} = \frac{1}{6} \sum_{\alpha\beta} V_{\alpha\beta} Q_{\alpha\beta} \tag{4.10}$$

4.2 Quantum mechanical formalism

The Hamiltonian

To get the energy operator (the Hamiltonian) we should convert all the classical parameters to their quantum mechanics equivalent. The procedure is thoroughly described in chapter 10 of

ref [18] and yields the result

$$\hat{H}_q^{EFG} = \frac{\hbar\omega_0}{6}\left[3\hat{I}_z^2 - \hat{\mathbf{I}}^2 + \eta\left(\hat{I}_x^2 - \hat{I}_y^2\right)\right] \tag{4.11}$$

where

$$\omega_0 \triangleq \frac{3e^2qQ}{2I(2I-1)\hbar} \tag{4.12}$$

The superscript "EFG" denotes that this Hamiltonian is in a reference frame defined by the direction of the diagonal EFG tensor, where I is the total angular momentum operator, and $Q \propto \left\langle m_I = I, I \left| 3z_z^2 - \mathbf{r}^2 \right| I, m_I = I \right\rangle$ is the quadrupole moment of the nucleus.

The idea of this conversion is to transform classical quantities to their quantum analog operators, and then to transform those operators to a more convenient set of operators. The classical quantities are x, y, z, their quantum mechanical analog are the coordinate operators. But since for each nucleon its location is connected to its orbital angular momentum (for example $l_x = \frac{1}{i}\left(y\frac{\partial}{\partial z} - z\frac{\partial}{\partial y}\right)$) we can convert the coordinate operators to the angular momentum operators, which are convenient operators to deal with. (The connection between the two sets of operators is possible because they are both sets of tensors of rank two and the transformation is done formally by using the Wigner-Eckart theorem [19]). This intuitive picture helps us to understand the meaning of Q. Since the theorem shows us that the two sets of operators have proportional matix elements, and since we are interested in the energy (which is known up to a constant) the linear connection must depend on the difference between states in the two sets. This is illustrated in Fig 4-1. In this figure the left set is related to the quadrupole energy levels in the coordinates representation, while the right one refers to the angular momentum basis. The connection is

$$(E_1 + a)\,C = (U_1 + b) \quad , \quad (E_2 + a)\,C = (U_2 + b) \qquad \Longrightarrow \qquad C = \frac{U_2 - U_1}{E_2 - E_1}$$

but since we measure U, this constant is proportional to $E_2 - E_1$. Namely, this constant depends on the difference between two states in the coordinate representation, which is exactly the form of Q. It means then that Q has the meaning of a scaling factor.

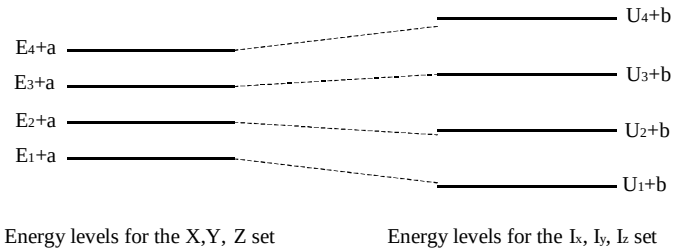

Figure 4-1: The Wigner-Eckhart theorem connects the coordinate representation to the angular momentum representation by a constant.

For spin $\frac{3}{2}$ (the copper's nucleus spin) the standard basis is

$$\begin{aligned} \langle 3/2| &= \begin{pmatrix} 1 & 0 & 0 & 0 \end{pmatrix} \qquad \langle 1/2| = \begin{pmatrix} 0 & 1 & 0 & 0 \end{pmatrix} \\ \langle -1/2| &= \begin{pmatrix} 0 & 0 & 1 & 0 \end{pmatrix} \qquad \langle -3/2| = \begin{pmatrix} 0 & 0 & 0 & 1 \end{pmatrix} \end{aligned} \tag{4.13}$$

$$\hat{\mathbf{I}} = \left[\begin{pmatrix} 0 & \frac{\sqrt{3}}{2} & 0 & 0 \\ \frac{\sqrt{3}}{2} & 0 & 1 & 0 \\ 0 & 1 & 0 & \frac{\sqrt{3}}{2} \\ 0 & 0 & \frac{\sqrt{3}}{2} & 0 \end{pmatrix}, \begin{pmatrix} 0 & -i\frac{\sqrt{3}}{2} & 0 & 0 \\ i\frac{\sqrt{3}}{2} & 0 & -i & 0 \\ 0 & i & 0 & -i\frac{\sqrt{3}}{2} \\ 0 & 0 & i\frac{\sqrt{3}}{2} & 0 \end{pmatrix}, \begin{pmatrix} 3/2 & 0 & 0 & 0 \\ 0 & 1/2 & 0 & 0 \\ 0 & 0 & -1/2 & 0 \\ 0 & 0 & 0 & -3/2 \end{pmatrix} \right] \tag{4.14}$$

and the matrix representation of 4.11 in this basis is

$$\hat{H}_q^{EFG} = \frac{\omega_0 \hbar}{6} \begin{pmatrix} 3 & 0 & \eta\sqrt{3} & 0 \\ 0 & -3 & 0 & \eta\sqrt{3} \\ \eta\sqrt{3} & 0 & -3 & 0 \\ 0 & \eta\sqrt{3} & 0 & 3 \end{pmatrix} \tag{4.15}$$

Diagonal form of the Hamiltonian

The matrix that diagonalizes $\hat{H}_q^{EFG}$ is

$$T = \frac{1}{\sqrt{1+\sigma^2}} \begin{pmatrix} 1 & 0 & \sigma & 0 \\ 0 & 1 & 0 & -\sigma \\ -\sigma & 0 & 1 & 0 \\ 0 & \sigma & 0 & 1 \end{pmatrix} \tag{4.16}$$

Where ς and σ are defined as

$$\sigma \triangleq \frac{\eta}{\sqrt{3}(1+\varsigma)} \quad , \quad \varsigma \triangleq \sqrt{1+\frac{\eta^2}{3}} \tag{4.17}$$

And the diagonal form is

$$\hat{H}_q^{diagonal} = T\hat{H}_q^{EFG}T^{\dagger} = \frac{\omega_0\hbar\varsigma}{2} \begin{pmatrix} 1 & 0 & 0 & 0 \\ 0 & -1 & 0 & 0 \\ 0 & 0 & -1 & 0 \\ 0 & 0 & 0 & 1 \end{pmatrix} \tag{4.18}$$

We therefore conclude that our system is composed of two doublets of energy.

$$E_{\mp\frac{1}{2}} = -\frac{\omega_0\hbar\varsigma}{2} \quad , \quad E_{\mp\frac{3}{2}} = \frac{\omega_0\hbar\varsigma}{2}$$

4.2.1 Interaction with an external time dependent magnetic field

We now add, like in the spin $\frac{1}{2}$ case (appendix A), an interaction with an external time dependent magnetic field. Since the reference frame of the problem is defined by the three principal axes of the EFG tensor, orienting the coil in an arbitrary direction of space yields a magnetic field of the form

$$\mathbf{B}(t) = 2B_1\cos(\omega t)\left[\sin(\theta)\cos(\phi), \sin(\theta)\sin(\phi), \cos(\theta)\right] \tag{4.19}$$

This field defines another characteristic frequency in the system

$$\omega_1 \triangleq \gamma B_1 \tag{4.20}$$

and the Hamiltonian becomes $\hat{H}^{EFG}(t) = \hat{H}_q^{EFG} + \hat{W}^{EFG}(t)$ with

$$\begin{aligned}
\hat{W}^{EFG}(t) &= 2\hbar\omega_1 \cos(\omega t)\cos(\theta) \begin{pmatrix} \frac{3}{2} & 0 & 0 & 0 \\ 0 & \frac{1}{2} & 0 & 0 \\ 0 & 0 & -\frac{1}{2} & 0 \\ 0 & 0 & 0 & -\frac{3}{2} \end{pmatrix} \\
&\quad +2\hbar\omega_1 \cos(\omega t)\sin(\theta) \begin{pmatrix} 0 & \frac{\sqrt{3}}{2}e^{-i\phi} & 0 & 0 \\ \frac{\sqrt{3}}{2}e^{i\phi} & 0 & e^{-i\phi} & 0 \\ 0 & e^{i\phi} & 0 & \frac{\sqrt{3}}{2}e^{-i\phi} \\ 0 & 0 & \frac{\sqrt{3}}{2}e^{i\phi} & 0 \end{pmatrix}
\end{aligned} \tag{4.21}$$

Since we've transformed $\hat{H}_q^{EFG}$ to a diagonal form we must apply the same transformation to the perturbation part ($\hat{W}^{diagonal}(t) = T\hat{W}^{EFG}(t)T^{\dagger}$), a calculation that ends with

$$\begin{aligned}
\hat{W}^{diagonal}(t) &= \frac{2\hbar\omega_1 \cos(\omega t)}{1+\sigma^2}\cos(\theta) \begin{pmatrix} \frac{3}{2}-\frac{\sigma^2}{2} & 0 & -2\sigma & 0 \\ 0 & \frac{1}{2}-\frac{3\sigma^2}{2} & 0 & 2\sigma \\ -2\sigma & 0 & -\frac{1}{2}+\frac{3\sigma^2}{2} & 0 \\ 0 & 2\sigma & 0 & -\frac{3}{2}+\frac{\sigma^2}{2} \end{pmatrix} \\
&\quad +\frac{2\hbar\omega_1 \cos(\omega t)}{1+\sigma^2}\sin(\theta) \begin{pmatrix} 0 & D^* & 0 & F^* \\ D & 0 & E^* & 0 \\ 0 & E & 0 & D^* \\ F & 0 & D & 0 \end{pmatrix}
\end{aligned} \tag{4.22}$$

Where D, E and F are defined as

$$\begin{aligned} D &\triangleq \frac{\sqrt{3}}{2}e^{i\phi}\left[1-\sigma^2+\frac{2}{\sqrt{3}}\sigma e^{-2i\phi}\right] \triangleq D_0 e^{i\lambda} \\ E &\triangleq e^{i\phi}\left[1-\sigma\sqrt{3}e^{-2i\phi}\right] \\ F &\triangleq \frac{\sqrt{3}}{2}e^{i\phi}\left[2\sigma+\frac{2}{\sqrt{3}}\sigma^2 e^{-2i\phi}\right] \end{aligned} \tag{4.23}$$

Since $\frac{\omega_0}{\omega_1} \approx 100$ the diagonal elements of Eq 4.22 are much smaller than those of Eq 4.18 and we omit them. Furthermore, according to the off resonance approximation (see footnote in appendix A) we can also omit the terms with E and F since a time dependent perturbation can not couple degenerate energy levels. Our Hamiltonian is thus reduced to

$$\begin{aligned} \hat{H}^{diagonal}(t) &= \frac{\omega_0\hbar\varsigma}{2}\begin{pmatrix} 1 & 0 & 0 & 0 \\ 0 & -1 & 0 & 0 \\ 0 & 0 & -1 & 0 \\ 0 & 0 & 0 & 1 \end{pmatrix} + \\ & \frac{2\hbar\omega_1 D_0\cos(\omega t)}{1+\sigma^2}\begin{pmatrix} 0 & e^{-i\lambda}\sin(\theta) & -\frac{2\sigma}{D_0}\cos(\theta) & 0 \\ e^{i\lambda}\sin(\theta) & 0 & 0 & \frac{2\sigma}{D_0}\cos(\theta) \\ -\frac{2\sigma}{D_0}\cos(\theta) & 0 & 0 & e^{-i\lambda}\sin(\theta) \\ 0 & \frac{2\sigma}{D_0}\cos(\theta) & e^{i\lambda}\sin(\theta) & 0 \end{pmatrix} \end{aligned}$$

By using the definitions of Eq 4.23, 4.17 and the following new ones

$$\mathbf{a} \triangleq \frac{1}{2\sqrt{3+\eta^2}}(\eta+3, \eta-3, 2\eta) \tag{4.24}$$

$$A_{\pm} \triangleq a_x\cos(\phi) \pm i a_y \sin(\phi) \quad , \quad A_z \triangleq a_z \tag{4.25}$$

$$\epsilon \triangleq \sqrt{A_+ A_- \sin^2(\theta) + A_z^2\cos^2(\theta)} \tag{4.26}$$

$\hat{H}^{diagonal}(t)$ can be written in a more convenient way

$$\hat{H}^{diagonal}(t) = \frac{\omega_0 \hbar \varsigma}{2} \begin{pmatrix} 1 & 0 & 0 & 0 \\ 0 & -1 & 0 & 0 \\ 0 & 0 & -1 & 0 \\ 0 & 0 & 0 & 1 \end{pmatrix} + 2\hbar\omega_1 \cos(\omega t) \begin{pmatrix} 0 & A_+ \sin(\theta) & -A_z \cos(\theta) & 0 \\ A_- \sin(\theta) & 0 & 0 & A_z \cos(\theta) \\ -A_z \cos(\theta) & 0 & 0 & A_+ \sin(\theta) \\ 0 & A_z \cos(\theta) & A_- \sin(\theta) & 0 \end{pmatrix} \quad (4.27)$$

The wave function

We seek a wave function that fulfills Schrödinger's equation with the Hamiltonian of Eq 4.27. We start with

$$\Psi^{diagonal}(t) = \begin{pmatrix} e^{-i\frac{\omega_0 \varsigma}{2}t} & 0 & 0 & 0 \\ 0 & e^{i\frac{\omega_0 \varsigma}{2}t} & 0 & 0 \\ 0 & 0 & e^{i\frac{\omega_0 \varsigma}{2}t} & 0 \\ 0 & 0 & 0 & e^{-i\frac{\omega_0 \varsigma}{2}t} \end{pmatrix} \varphi(t) \triangleq \hat{U}_0^{NQR}(t)\varphi(t) \quad (4.28)$$

and notice that $\hat{U}_0^{NQR}(t)$ is no more than the time propagator for the Hamiltonian without the perturbation (Eq 4.18). Inserting this wave function into Schrödinger's equation, choosing $\omega = \omega_0$, and using the off resonance approximation (see footnote in appendix A) gives us Schrödinger's equation $i\hbar\frac{\partial}{\partial t}\varphi = \hat{H}^{\varphi}\varphi$ with the Hamiltonian

$$\hat{H}^{\varphi} = \hbar\omega_1 \begin{pmatrix} 0 & A_+ \sin(\theta) & -A_z \cos(\theta) & 0 \\ A_- \sin(\theta) & 0 & 0 & A_z \cos(\theta) \\ -A_z \cos(\theta) & 0 & 0 & A_+ \sin(\theta) \\ 0 & A_z \cos(\theta) & A_- \sin(\theta) & 0 \end{pmatrix} \quad (4.29)$$

Unlike Eq 4.27 this Hamiltonian is time independent, which means that the solution for $\varphi(t)$ is

$$\varphi(t) = \exp^{-\frac{i}{\hbar}\hat{H}^{\varphi}t}\,\varphi(0) \tag{4.30}$$

An explicit solution for the exponential operator of Eq 4.30 is achieved by finding a matrix S such that $\hat{H}^{\varphi}_{diagonal} = S\hat{H}^{\varphi}S^{\dagger}$ is diagonal, and the solution is then

$$\varphi(t) = S^{\dagger}\exp^{-\frac{i}{\hbar}\hat{H}^{\varphi}_{diagonal}t}\,S\varphi(0) \triangleq \hat{U}_{pulse}(t)\varphi(0) \tag{4.31}$$

The explicit forms of those matrixes are

$$S = \frac{1}{2\epsilon}\begin{pmatrix} \epsilon & A_+\sin(\theta) + A_z\cos(\theta) & A_-\sin(\theta) - A_z\cos(\theta) & \epsilon \\ -\epsilon & A_+\sin(\theta) + A_z\cos(\theta) & A_-\sin(\theta) - A_z\cos(\theta) & -\epsilon \\ \epsilon & -A_+\sin(\theta) + A_z\cos(\theta) & A_-\sin(\theta) + A_z\cos(\theta) & -\epsilon \\ -\epsilon & -A_+\sin(\theta) + A_z\cos(\theta) & A_-\sin(\theta) + A_z\cos(\theta) & \epsilon \end{pmatrix} \tag{4.32}$$

$$\hat{H}^{\varphi}_{diagonal} = \frac{\epsilon\hbar\omega_1}{2}\begin{pmatrix} 1 & 0 & 0 & 0 \\ 0 & -1 & 0 & 0 \\ 0 & 0 & -1 & 0 \\ 0 & 0 & 0 & 1 \end{pmatrix} \tag{4.33}$$

$$\hat{U}_{pulse}(t) = \frac{\sin(\epsilon\omega_1 t)}{\epsilon}\begin{pmatrix} \epsilon\cot(\epsilon\omega_1 t) & -iA_+\sin(\theta) & iA_z\cos(\theta) & 0 \\ -iA_-\sin(\theta) & \epsilon\cot(\epsilon\omega_1 t) & 0 & -iA_z\cos(\theta) \\ iA_z\cos(\theta) & 0 & \epsilon\cot(\epsilon\omega_1 t) & -iA_+\sin(\theta) \\ 0 & -iA_z\cos(\theta) & -iA_-\sin(\theta) & \epsilon\cot(\epsilon\omega_1 t) \end{pmatrix} \tag{4.34}$$

The operator $\hat{U}_{pulse}(t)$, as it is defined in Eq 4.31, is the time propagator of the system during the RF pulse.

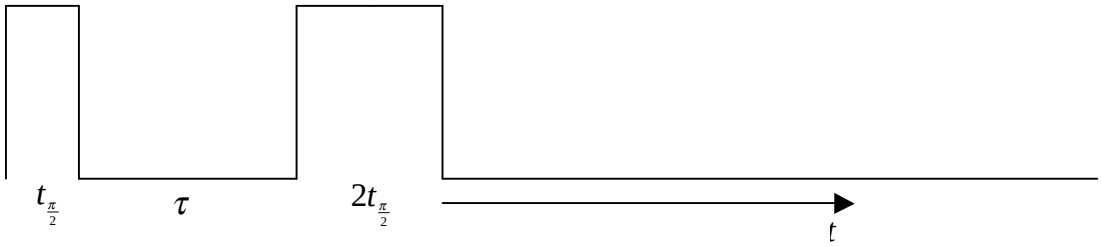

Figure 4-2: Schematic description of a spin echo sequence. Two pulses, $\frac{\pi}{2}$ and π, seperated by a pause of time τ. For more details see appendix C.

We can know write the full wave function as

$$\Psi^{diagonal}(t) = \hat{U}_0^{NQR}(t)\varphi(t) = \hat{U}_0^{NQR}(t)\hat{U}_{pulse}(t)\varphi(0) \tag{4.35}$$

This result is the analog of Eq A.28 . For a more comprehensive example see appendix B.

4.3 Magnetization after a spin echo sequence

Total magnetization

We now want to calculate the average magnetization vector after applying a "Spin Echo" sequence. Applying Eq 4.35 to this case gives

$$\Psi_{echo}^{EFG}(t + 2t_{\frac{\pi}{2}} + \tau + t_{\frac{\pi}{2}}) = T^{\dagger}\hat{U}_0^{NQR}(t + 2t_{\frac{\pi}{2}})\hat{U}_{pulse}(2t_{\frac{\pi}{2}})\hat{U}_0^{NQR}(\tau + t_{\frac{\pi}{2}})\hat{U}_{pulse}(t_{\frac{\pi}{2}})\varphi(0) \triangleq \hat{U}_{echo}\varphi(0) \tag{4.36}$$

were the term $T^{\dagger}$ is used to transform the wave function back to the EFG reference frame. This sequence is described in Fig 4-2.

The state $\varphi(0)$ is one of the eigenstates of the Hamiltonian $\hat{H}_q^{diagonal}$ (Eq 4.18). By considering the thermal population of each eigenstate in equilibrium we find the average magnetization

to be

$$\begin{aligned}\left\langle \mathbf{M}^{EFG}(t)\right\rangle &= \frac{2\gamma}{\epsilon}\left(\sin(\theta)\cos(\phi)a_x^2,\sin(\theta)\sin(\phi)a_y^2,\cos(\theta)a_z^2\right)\times\left[\frac{e^{-\frac{\hbar\omega_{0\varsigma}}{2KT}}-e^{+\frac{\hbar\omega_{0\varsigma}}{2KT}}}{Z}\right]\\ &\times\left[\begin{array}{c}\sin\left(4\epsilon\omega_1 t_{\frac{\pi}{2}}\right)\cos(2\epsilon\omega_1 t_{\frac{\pi}{2}})\sin(\omega_{0\varsigma}(t+2t_{\frac{\pi}{2}}))\\ +\sin^3(2\epsilon\omega_1 t_{\frac{\pi}{2}})\sin(\omega_{0\varsigma}(\tau-t_{\frac{\pi}{2}}-t))\\ +\sin\left(2\epsilon\omega_1 t_{\frac{\pi}{2}}\right)\cos^2(2\epsilon\omega_1 t_{\frac{\pi}{2}})\sin(\omega_{0\varsigma}(\tau+3t_{\frac{\pi}{2}}+t))\end{array}\right]\end{aligned}\tag{4.37}$$

Where $Z=2\left(e^{-\frac{\hbar\omega_{0\varsigma}}{2KT}}+e^{+\frac{\hbar\omega_{0\varsigma}}{2KT}}\right)$ is the partition function of the system, K is the Boltzman constant and T is the temperature.

Dephasing effect

The dispersion of a wave group while propagating in a dispersive medium is a well known phenomena. The basic idea is that different frequencies of the group propagate with different velocities, and as a consequence they start losing phase. This means that there is a destructive interference between the modes of the group and with time the group becomes wider and smaller in amplitude. The same effect happens here. Eq 4.37 describes a single spin in the sample with a velocity (in our case angular, and not linear, velocity) $\omega_{0\varsigma}$. Since our sample is not perfectly homogenous there are spins with different environments, namely different EFG tensors, which mean different $q's$ (Eq 4.7). But this, in turn, means different angular velocities as can be deduced from Eq 4.12. Therefore, if we want to calculate the total signal of the sample we must sum over all the spins in the sample. By assuming a normal distribution of frequencies around an average value ϖ_0, we can obtain the result

$$\begin{aligned}\left\langle \mathbf{M}^{EFG}(t)\right\rangle &\propto \frac{2}{\epsilon}\left(\sin(\theta)\cos(\phi)a_x^2,\sin(\theta)\sin(\phi)a_y^2,\cos(\theta)a_z^2\right)\times\\ &\int_{-\infty}^{\infty}d\omega_0 e^{-\left(\frac{\omega_0-\varpi_0}{\delta}\right)^2}\left[\begin{array}{c}\sin\left(4\epsilon\omega_1 t_{\frac{\pi}{2}}\right)\cos(2\epsilon\omega_1 t_{\frac{\pi}{2}})\sin(\omega_{0\varsigma}(t+2t_{\frac{\pi}{2}}))\\ +\sin^3(2\epsilon\omega_1 t_{\frac{\pi}{2}})\sin(\omega_{0\varsigma}(\tau-t_{\frac{\pi}{2}}-t))\\ +\sin\left(2\epsilon\omega_1 t_{\frac{\pi}{2}}\right)\cos^2(2\epsilon\omega_1 t_{\frac{\pi}{2}})\sin(\omega_{0\varsigma}(\tau+3t_{\frac{\pi}{2}}+t))\end{array}\right]\end{aligned}$$

which yields the expression

$$\begin{aligned}\left\langle \mathbf{M}^{EFG}(t)\right\rangle \quad \propto \quad & \frac{2}{\epsilon}\left(\sin(\theta)\cos(\phi)a_x^2,\sin(\theta)\sin(\phi)a_y^2,\cos(\theta)a_z^2\right)\times \\ & \left[\begin{array}{c} \sin\left(4\epsilon\omega_1 t_{\frac{\pi}{2}}\right)\cos(2\epsilon\omega_1 t_{\frac{\pi}{2}})\sin(\varpi_0\varsigma(t+2t_{\frac{\pi}{2}}))\exp\left\{-\frac{\zeta^2\delta^2(t+2t_{\frac{\pi}{2}})^2}{4}\right\} \\ +\sin^3(2\epsilon\omega_1 t_{\frac{\pi}{2}})\sin(\varpi_0\varsigma(\tau-t_{\frac{\pi}{2}}-t))\exp\left\{-\frac{\zeta^2\delta^2(\tau-t_{\frac{\pi}{2}}-t)^2}{4}\right\}+ \\ \sin\left(2\epsilon\omega_1 t_{\frac{\pi}{2}}\right)\cos^2(2\epsilon\omega_1 t_{\frac{\pi}{2}})\sin(\varpi_0\varsigma(\tau+3t_{\frac{\pi}{2}}+t))\exp\left\{-\frac{\zeta^2\delta^2(\tau+3t_{\frac{\pi}{2}}+t)^2}{4}\right\}\end{array}\right]\end{aligned}$$

The last result means that we got three gaussian shaped peaks centered at times $t=-2t_{\frac{\pi}{2}}$, $t=\tau-t_{\frac{\pi}{2}}$, $t=-\tau-3t_{\frac{\pi}{2}}$ with a width of $\frac{2}{\zeta\delta}$. In practice this width is of the order of μsec, and since we are able to practically detect signal only some μsec after the second pulse ends, we conclude that the only detectable peak is the one centered at $t=\tau-t_{\frac{\pi}{2}}$. We therefore conclude that the measured signal is proportional to

$$\begin{aligned}\left\langle \mathbf{M}^{EFG}(t)\right\rangle \quad \propto \quad & \sin^3(2\epsilon\omega_1 t_{\frac{\pi}{2}})\exp\left\{-\frac{\zeta^2\delta^2(\tau-t_{\frac{\pi}{2}}-t)^2}{4}\right\} \\ & \times\frac{2}{\epsilon}\left(\sin(\theta)\cos(\phi)a_x^2,\sin(\theta)\sin(\phi)a_y^2,\cos(\theta)a_z^2\right)\end{aligned} \tag{4.38}$$

Magnetization in the coil direction

Eq 4.38 gives us the magnetization vector, with the dephasing effect, with respect to the EFG reference frame. Since the measured signal includes only the component of the magnetization in the coil direction we must project the total magnetization vector on this direction. The angles that define the orientation of the coil with respect to the EFG reference frame were defined in Eq 4.19, and by using Eq 4.26 we obtain the expression

$$\left\langle \mathbf{M}^{coil}(t)\right\rangle \propto \epsilon\sin^3(2\epsilon\omega_1 t_{\frac{\pi}{2}})\exp\left\{-\frac{\zeta^2\delta^2(\tau-t_{\frac{\pi}{2}}-t)^2}{4}\right\} \tag{4.39}$$

Optimization of the pulse length

Eq 4.39 gives us the magnetization in the coil as a function of θ,ϕ and η . We shall study a special case in which V_{zz} at each point of the sample has the same direction. In other words, this is a case where we can define a clear direction in space, which we denote as z, and in

each point of the sample the largest component of the EFG tensor (V_{zz}) will point toward this direction. In this case the other two components of the tensor, at each point of the sample, have random directions in the plane perpendicular to z . It means then that the xy plane is degenerate and we must integrate over all the possible values of ϕ, namely

$$\left\langle \mathbf{M}^{coil}(t) \right\rangle (\theta, \eta) \propto \int_0^{2\pi} \epsilon \sin^3(2\omega_1 t_{\frac{\pi}{2}} \epsilon) d\phi \tag{4.40}$$

where we have chosen to measure the signal value at the peak of the gaussian shaped envelope, a common procedure for a spin echo experiment. The optimization of the pulse length is a preparation stage where we tune the pulse length ($t_{\frac{\pi}{2}}$) to a value which yields the maximum signal intensity. This is done with $\theta = \frac{\pi}{2}$ (the configuration with the strongest signal). We therefore conclude that the optimum $t_{\frac{\pi}{2}}$ value can be found by finding the maxima of

$$\int_0^{2\pi} \sqrt{\cos^2(\phi) a_x^2 + \sin^2(\phi) a_y^2} \times \sin^3 \left(2\omega_1 t_{\frac{\pi}{2}} \sqrt{\cos^2(\phi) a_x^2 + \sin^2(\phi) a_y^2} \right) d\phi$$

with respect to $t_{\frac{\pi}{2}}$. Solving the problem numerically yields the solution $\omega_1 t_{\frac{\pi}{2}} = 0.90728$ for the first maximum, which was also found to be weakly dependent on η (Fig 4-3).

4.4 Summary

Eq 4.40 means that for a NQR spin echo experiment the signal intensity depends on θ and η. The idea of the ADNQR technique is based on this effect.

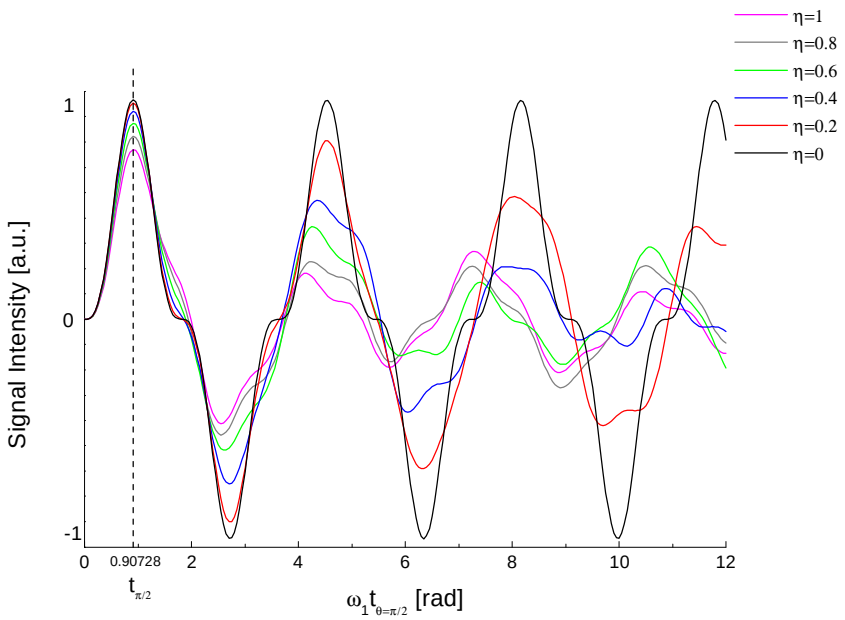

Figure 4-3: The echo intensity, for $\theta = \frac{\pi}{2}$, as a function of the pulse length. The optimal value, $t_{\frac{\pi}{2}}$, was determined from the first maximum, and is independent of η.

Chapter 5

$YBCO$ - Structure and properties

The high-T_c superconductors are classified in a few groups according to their chemical formulas. A common property to all of them is the presence of CuO_2 planes which play a major role in the superconducting mechanism. Our work focuses on a specific group - $YBCO_y$. In this chapter we intend to give a short description of the $YBCO_y$ structure and properties. We will concentrate on those properties that are relevant for NQR measurements.

The notation $YBCO_y$ is the abbreviation for the superconducting group which has the chemical formula $Y_1Ba_2Cu_3O_{6\leq y\leq 7}$. Fig 5-1 describes the unit cell of the two extreme cases of $YBCO$.

The visible change that oxygenation creates is to vary the amount of oxygen in the chains. Other parameters that depend on y are the lattice constants (an effect which is not illustrated in Fig 5-1). The most significant effect is the change of the shape of the unit cell from orthorhombic to tetragonal. In Fig 5-2 we see how doping affects those parameters.

In crystal form Y has a valence of +3, Ba of +2 and O of -2. The $Cu(1)$ valence is +1, and we therefore conclude that the $Cu(2)$ valence changes between +2 to +3 with increasing y. The fact that we can think of the Cu^{3+} as if it is in a close shell electron configuration implies that its electronic spin is zero (see ref [25]), while the Cu^{2+} ion has a non vanishing electronic spin. In neutron scattering experiments it was found that CuO_2 planes with Cu^{2+} ions are antiferromagnetic. In contrary to this situation, a CuO_2 plane composed of many non magnetic Cu^{3+} ions behaves as a metallic material. For intermediate values of y we can therefore conclude that each plane is like an array of magnetic moments (Cu^{2+} ions) with holes

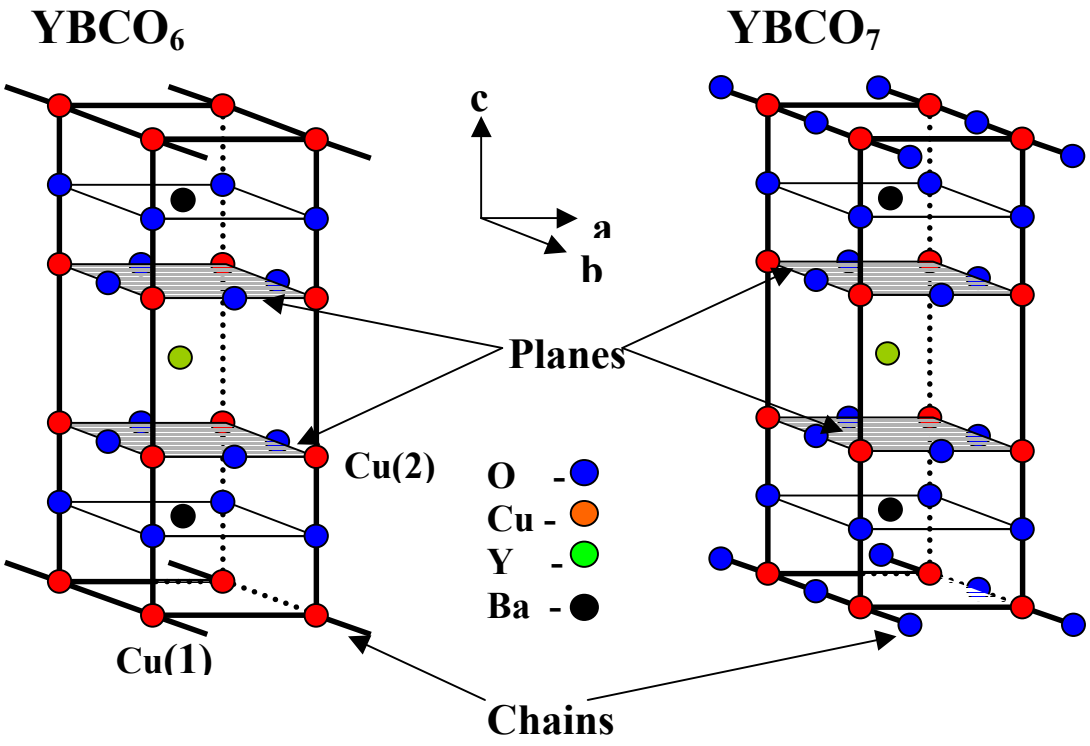

Figure 5-1: YBCO structure and notation

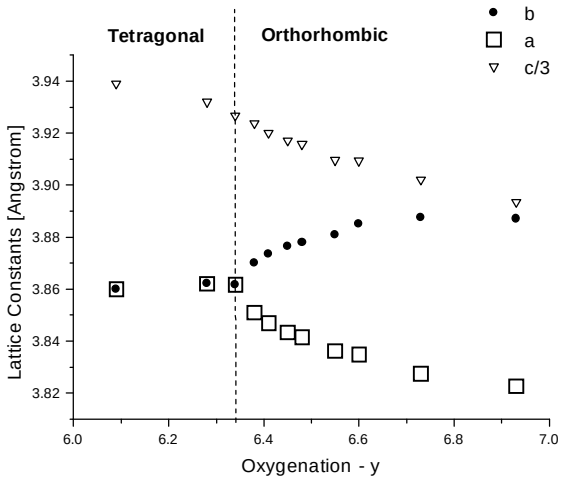

Figure 5-2: Lattice parameters of YBCO vs. oxygenation at room temperature. [9]

among them due to the non magnetic ions (Cu^{3+}). For our case, the important effects of the valence changes are the presence of magnetic domains and the change of the ions charge.

As we saw in chapter 1, the local symmetry is important because it affects the electric field gradient (EFG) tensor around the ions. We are therefore interested in the tensor symmetry around the copper ions. We start with the $Cu(2)$ ions. For $y = 7$ the planes are asymmetric since $a \neq b$ (the orthorhombic phase), and the copper ions of the plane hold a charge of $+3$ or $+2$. For $y = 6$ the planes become symmetric ($a = b$) and the charge of the $Cu(2)$ is now $+2$. In the c direction the decrease in y value is accompanied by an increase of the distance between the $Cu(2)$ ion and its neighboring oxygen and $Cu(2)$ ions. The trend of those two effects (charge and distance changes) is expected to decrease V_{zz} and therefore to reduce the resonance frequency, ω_0, as y is reduced (Eq 4.7). This effect indeed exist, as can be seen in Fig 2-3. For the $Cu(1)$ ions in the $y = 6$ case we have full symmetry in the ab plane, while the c direction differs much from this plane. On the other hand, the $y = 7$ case is crucially different, because now the bc planes are symmetric (with respect to the $Cu(1)$ ions) and the a axis is different.

The phase diagram is shown is Fig 5-3. The horizontal axis indicates the oxygenation level. The left axis gives a temperature scale (T_N) that refers to the magnetic properties of

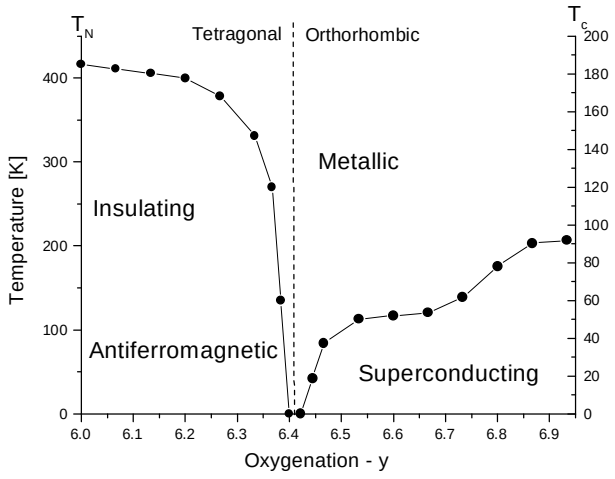

Figure 5-3: Phase diagram of YBCO

the $YBCO$. The magnetic zone is bounded by a line denoting the Neel's temperature. This is the temperature where the material starts to undergo a magnetic phase transition, from an homogenous dynamic antiferromagnet with zero net magnetization, to an inhomogeneous structure that includes domains of antiferromagnet with non zero net magnetization. This means that for low values ($y \leq 6.4$) of doping each ion in the sample feels a large magnetic field, an effect that drastically change the NQR measurement. The right axis refers to the T_c temperature, the temperature at which the superconducting phase transition occurs. The structural phase transition occurs at $y = 6.4$.

Chapter 6

Sample preparation and characterization

In this chapter we describe the samples preparation and characterization process.

6.1 Preparation

1. We used a 99.9% pure YBCO powder, manufactured by PRAXAIR.
2. Its doping level was measured by iodometry titration.
3. The powder grains size was about 5μm .
4. We inserted $1.095g$ of the powder into a teflon cylinder of length 10.3mm and 9.5mm in diameter, and mixed it with StayCast glue.
5. The sample was immediately inserted into a magnetic field of $8.0033T$.
6. During the first 30 minutes in the field the sample was shaked by connecting it to a 70cm rod which was connected to an electromagnetic relay. The input voltage to the relay was a 25Hz square wave.
7. After 30 minutes the vibrations were stopped and the sample was left to dry for about 12 hours inside the magnetic field.

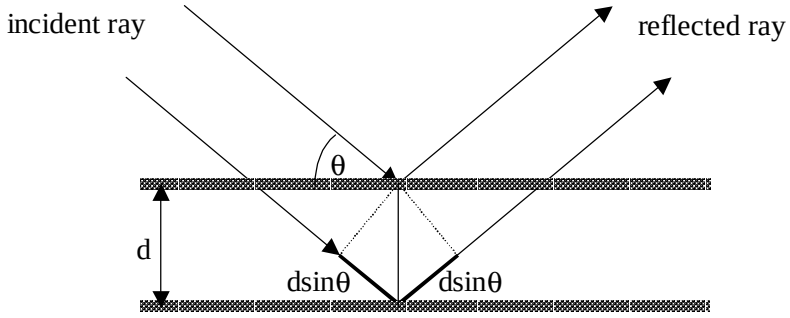

Figure 6-1: Interference by reflection from two parallel planes. When the optical length difference - $2dsin\theta$, is equal to a multiple of the wave length we receive the Bragg formula.

8. After removing the sample from the field and the teflon cylinder a line was marked on it to indicate the field direction.

Stages 4-8 describe the orientation procedure. In this process each tiny grain alters its orientation inside the glue while drying, till its c direction is parallel to the magnetic field. This is because the susceptibility of each grain, which is a single crystal, creates the maximum magnetic moment in the direction of the crystal c axis. We thus conclude that the orientation process aligns all the YBCO grains so that all the $(00l)$ planes are perpendicular to the magnetic field. Since the $(00l)$ planes are, by definition, parallel to the xy plane it is clear then that we identify the z direction with the magnetic field direction.

6.2 Characterization method : x-ray diffraction

The first parameter we measured was the doping level (stage 2 of the preparation section). To learn about the orientation quality we used x-ray diffraction. The method is based on the Bragg formula for constructive interference from crystal planes, as it is illustrated in Fig 6-1, and given by the expression

$$n\lambda = 2d\sin(\theta) \qquad \text{Bragg Formula}$$

where n is an integer and λ the wave length. We see then that the Bragg angle, θ, depends on the distance between parallel planes.

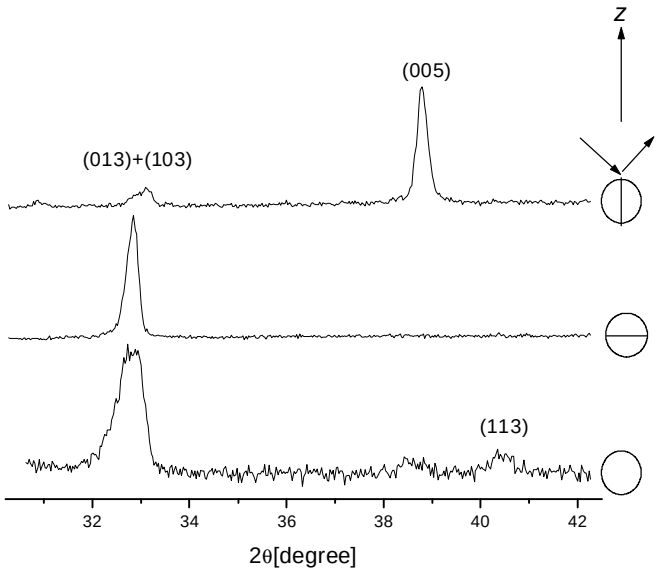

Figure 6-2: x-ray diffraction result of the $YBCO_7$ samples. Those samples were prepared by shaking. Lower graph, disoriented sample. Upper and middle, oriented sample.

Since the grains in the powder are randomly oriented, we expect to detect signals from all the angles that fulfill Bragg's formula. In an oriented sample we have a highly preferred plane family, the $(00l)$ one. We therefore expect to get a much stronger signal for the angles that refer to those planes.

In Fig 6-2 the lower graph describes the result of a x-ray experiment on $YBCO_7$ in a powder form. This sample was prepared according to stages 1-4 but without stages 5-8 (without orientation). The scan of this experiment, as well as the others, was focused on a narrow band of angles, for reasons we shall explain later. The result shows a strong and wide peak around $2\theta = 32.8°$. From reference data we know that this peak is related to reflection from (013) and (103) planes. The two small peaks at $38.5°$ and $40.5°$ are related to reflection from (005) and (113) respectively.

The upper graph of Fig 6-2 is the result of the oriented sample when the effective planes family is the $(00l)$ type. The sample configuration of this experiment is illustrated in Fig 6-3. In this figure the 9 joined unit cells represent a tiny grain of a single crystal. The fact that all the

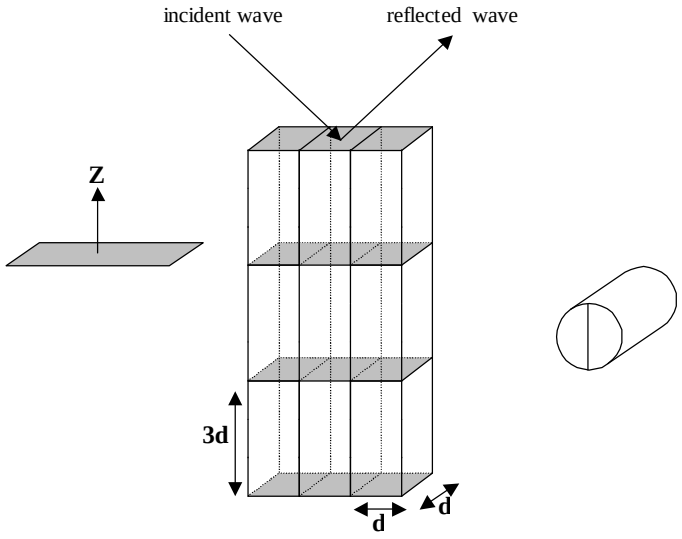

Figure 6-3: Each tiny grain of the powder is a single crystal, represented in this figure as 9 joined unit cells. The $(00l)$ planes are marked in gray, and are all parallel throughout the all sample. This plane direction is marked by a line on the sample, as illustrated in the right cylinder.

planes, other then the $(00l)$, are effectively in a powder form can be understood through this figure by gathering many such grains, all of which with parallel gray planes (the $(00l)$ planes), but with random rotation angles around the z axis. The cylinder in the right side of the figure describes the practical configuration of the sample in the experiment.

As can be seen in the graph the (005) peak was significantly enhanced. All the other peaks are almost undetectable with comparison to this one. After a 90 degrees rotation of the sample we expect the (005) peak to disappear, since its Bragg condition is unfulfilled, while the other should appear like in a normal powder case. This trend is indeed obtained in the middle graph.

Our ADNQR results were performed on samples that were not shake during orientation (without stage 6 in the preparation list). The relevant known details about them are there doping values; 7 and 6.675 and weight, 1g each. Fig 6-4 and 6-5 show the x-ray results of those samples. and we can see the same trend as before.

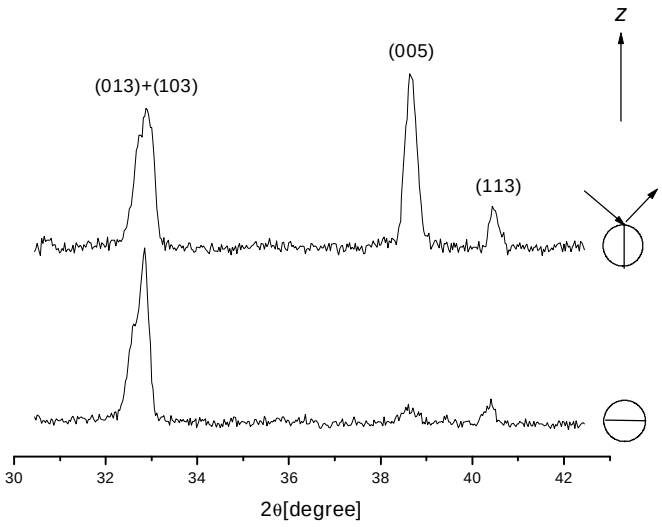

Figure 6-4: x-ray result of the $YBCO_7$ sample. This sample was prepared without shaking.

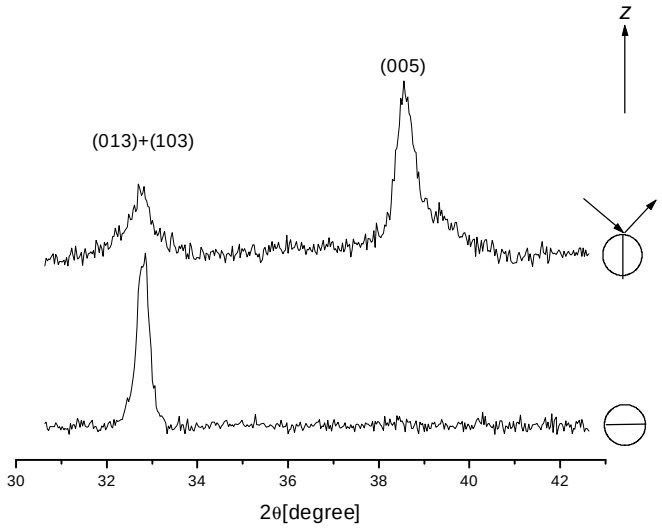

Figure 6-5: x-ray result of the $YBCO_{6675}$ sample. This sample was prepared without shaking.

6.2.1 Practical consideration for the x-ray experiment

As was mentioned before, the x-ray diffraction experiments were performed on a narrow band of the angle θ. The first criteria for choosing this range was based on the idea that the orientation process made the $(00l)$ planes family unique. We therefore searched for angles that corresponded to those planes. From the reference data for YBCO in powder form we know the reflection intensities for each peak. The reflection from the (002) planes, for instance, is four times stronger than the reflection from the (001) plane. ($(00l)$ means l equally spaced planes, in each unit cell, that are parallel to the ab plane). We also recall that in YBCO the unit cell dimensions have a ratio that is very close to 1:1:3 (see Fig 5-2). We therefore expect the planes (100) , (010) and (003) to correspond to the same angle θ, which is an undesired effect since it prevents us from detecting the (003) plane. Our second criteria was therefore to ignore all the planes with l that is a multiple of 3. The strongest peak that remained was (005) which is 13 times stronger than (001). The third criteria was to find upper and lower limits for θ. Since (103) is a clear strong peak related only to the powder nature of the spectrum (it is not from the family $(00l)$) and it is close to (005) we used it as our lower limit marker. A close, though not too strong, peak to be used as a limit from above is the (113) plane.

6.3 Summary

We were able to create samples of YBCO which have a preferred direction, the c axis direction. The quality of the orientation, namely what is the distribution of the alignment angles, is not clear from our characterization technique.

Chapter 7

Fit To Data

In chapter 2 we briefly introduced the experimental results. Indeed, we obtained an obvious angular dependence of the signal intensity, and a clear difference between different samples. In this chapter we intend to evaluate the exact asymmetry parameter (η) for the two samples of the preceding chapter.

7.1 Broadening effects

Eq 2.1 yields the theoretical line shape under the assumption of a perfectly aligned sample. In reality we expect to obtain a distribution of the grains alignment around the z axis, which can be inserted in the calculation by convoluting Eq 2.1 with a gaussian. Since we may be unable to estimate the width of this gaussian in a calibration experiment, we analyzed our data in a way that still makes our conclusions reliable. Our analysis goes as follows:

For the peak of $YBCO_7$ we assumed a single value for η and convoluted to Eq 2.3 with a gaussian, namely we calculated

$$\left\langle \mathbf{M}^{coil} \right\rangle (\theta, \eta) = \int_{\mathbf{0}}^{\pi} \left\langle \mathbf{M}^{coil} \right\rangle (\theta_{\mathbf{0}}, \eta)\, e^{-\left(\frac{\theta-\theta_0}{\sigma}\right)^2} d\theta_{\mathbf{0}}$$

We also multiplied this result by a factor that cancel the artificial normalization we applied to the theoretical result. By varying the width and the multiplying factor we improved the fit (in the sense of least squares). We then changed the value of η and repeated the process again

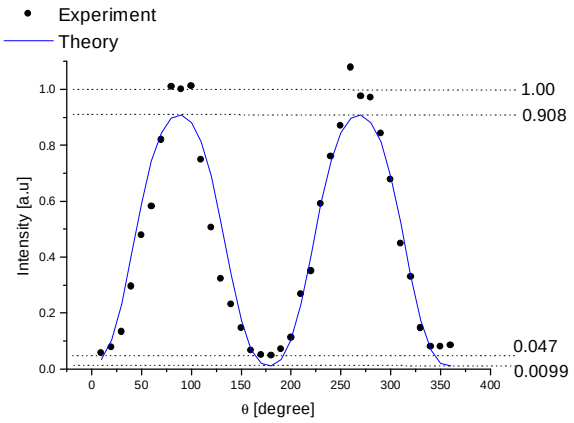

Figure 7-1: Theoretical and experimental results for the peak of $YBCO_7$. The line represent the best fit, including the broadening effect (see text). The fit results are $\eta = 0 \pm 0.1$ and $\sigma = 15°$. The RF frequency is 31.15MHz.

until we found the best fit. This yielded η and the distribution width.

For the shoulder of $YBCO_7$ and $YBCO_{6675}$ we used the width we found for $YBCO_7$, and varied η and the factor to obtain the optimum fits.

$YBCO_7$

In Fig 7-1 the result of such a fit for the $^{63}Cu(2)$ peak of $YBCO_7$ is presented. The parameters that correspond to the theoretical line are $\eta = 0 \pm 0.1$ and $\sigma = 15°$. This result agrees well with the known value of $\eta = 0.01 \pm 0.01$ as it appears in ref [17]. However, it should be noted that our experiment was performed at room temperature, while the cited value of η is for $4.2K$. Since the width parameter is speculated, in the sense that it doesn't necessarily indicate the real alignment distribution, we conclude that η is not absolutely correct. In other words, if the real alignment distribution is wider, η will be smaller. In Fig 7-2 we show the result for the $^{63}Cu(2)$ shoulder of $YBCO_7$.

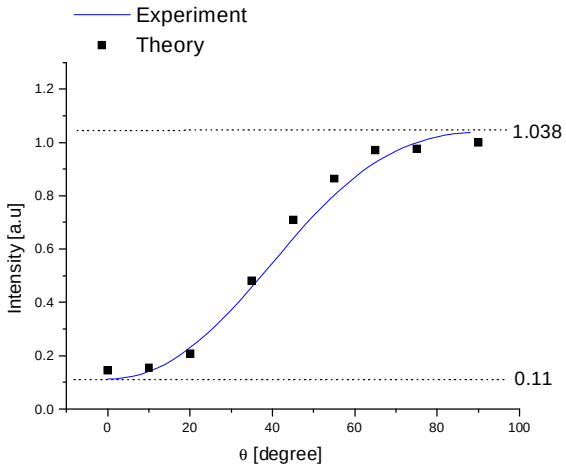

Figure 7-2: Theoretical and experimental results for the shoulder of $YBCO_7$. The line represent the best fit, including the broadening effect (see text). The fit results are $\eta = 0.6 \pm 0.1$ and $\sigma = 15°$. The RF frequency is 30.53MHz.

$YBCO_{6.675}$

For $YBCO_{6.675}$ the agreement of the result with the theory isnt as good as in the previous case. We recall that for $\eta = 1$ the minimum value is about 04 (see Fig 2-1), while in our data it's about 0.6. Such a significant change can be caused by an alignment distribution width of about 60°. The fact that the magnetic moment of $YBCO_{6675}$ is greater than that of $YBCO_7$ contradicts the conclusion that the alignment of $YBCO_{6.675}$ is wider than that of $YBCO_7$. In other word, using the width of 15° as an upper bound for the $YBCO_{6675}$ case does make sense. Fig 7-3 illustrates the fit of the parameters $\eta = 1 \pm 0.1$ and width=15° with the data.

7.2 Orientation of the EFG tensor

The EFG tensor includes two parameters η and q. They depend on the charges values, distances and symmetry. But in fact it includes more parameters - the orientation of the tensor with respect to the lattice axes. In this section we check whether these parameters can explain part of our data.

From Fig 5-1 we see that from a simple consideration of the ions position we expect $Cu(2)$

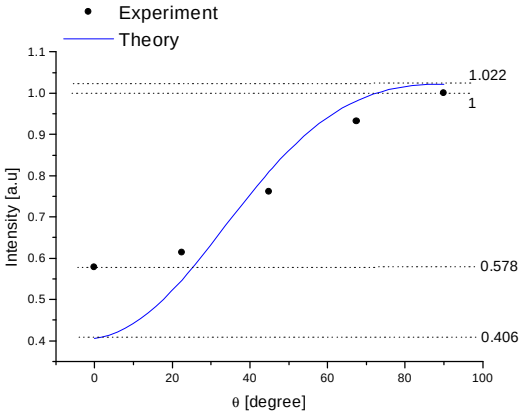

Figure 7-3: Theoretical and experimental results for $YBCO_{6675}$. The line represent the best fit, including the broadening effect with the same width as for the$YBCO_7$ case (see text). The fit result is $\eta = 1$. The RF frequency is 27.501MHz.

to have symmetry in the ab plane and preferred direction in the c axis, which is indeed the case. For the $Cu(1)$ case the same simple arguments can lead us to estimate that the EFG tensor at this point has its major axis in the a direction and that the bc plane is almost symmetric. This simple model fits the conclusion of [17]. We recall that the theoretical result, as it appears in Eq 2.1 underlies the assumption that the c axis is parallel to the V_{zz} direction, which is the case for $Cu(2)$ in $YBCO_7$, but not necessarily for $YBCO_{6.675}$.

7.2.1 Correction of the equation

In the frame of this work we didn't preform the calculation for this case - the case in which the direction of the orientation is not parallel to V_{zz}. What we will do is to explain the general influence of this effect. If the direction of the orientation (c) is parallel to the EFG major axis (V_{zz}) the magnetic field of the coil is given by (Eq 4.19).

$$\mathbf{B}(t) = 2B_1 \cos(\omega t)\,[\sin(\theta)\cos(\phi), \sin(\theta)\sin(\phi), \cos(\theta)] \tag{7.1}$$

as illustrated in the left part of Fig 7-4. In this case the a and b crystal axes are in the xy planes with arbitrary angles ϕ for each grain. If the direction of the orientation (c) is perpendicular

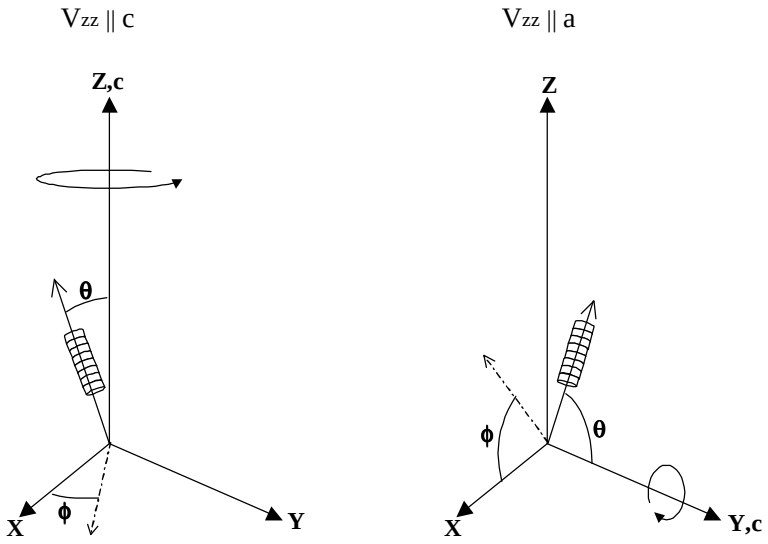

Figure 7-4: The coil orientation for different EFG orientations. Left: $V_{zz} \parallel c$ (as in $Cu(2)$ of $YBCO_7$). Right: $V_{zz} \parallel a$ (as in $Cu(1)$ of $YBCO_7$).

to the EFG major axis (V_{zz}) the coil magnetic field will be written as

$$\mathbf{B}(t) = 2B_1 \cos(\omega t) \left[\sin(\theta)\cos(\phi), \cos(\theta), \sin(\theta)\sin(\phi)\right] \tag{7.2}$$

which is the right case of Fig 7-4.

For the sake of simplicity we choose the case $\eta = 0$. Since the z component of $\mathbf{B}$ is irrelevant Eq 7.1 gives zero coupling value for $\theta = 0$ and maximum value for $\theta = \frac{\pi}{2}$, while from Eq 7.2 we see that the zero coupling value can not be obtained in the right case. The effect is probably more complicated since we have to integrate over ϕ.

We therefore suggest another effect that may help to explain the result of the $YBCO_{6.675}$ case. *If the orientation of the EFG tensor in $YBCO_{6.675}$ differs from the one of $YBCO_7$, we expect the signal intensity ratio of the $\theta = 0$ and $\theta = \frac{\pi}{2}$ cases to be smaller than the theoretical prediction we gave in chapter 2.* It is important to emphasize that this result coincides with our previous result of $\eta \approx 1$, since both of these effects imply that the symmetry in the planes of $YBCO_{6.675}$ is lower than the one of $YBCO_7$.

Chapter 8

Advantages and Disadvantages

The NMR methods to measure η use the quadrupole interaction as a perturbation that is added to a usual NMR Hamiltonain [1, 3, 10, 15, 16, 17, 18]. *Their basic idea is that different orientations of the EFG tensor, with respect to the NMR magnetic field, generate different energy levels.* Explicit calculation shows that the spectrum of such an Hamiltonain includes peaks from which one can deduce η. From hereafter we refer to this method as the NMR method. We compare now between the ADNQR method and the NMR method:

1. In a NQR experiment we measure the average value of η. Since ADNQR is sensitive to $|\eta|$, this method measure the average of $|\eta|$, which includes useful information that the average of η doesn't overlook. For the $|\eta|$ case zero average value means the sample is homogenous, while a non zero value clearly proves that inhomogeneity exists. On the other hand the NMR method, applied on a powder sample, gives peaks in the spectrum that depend linearly on η [10]. It means then that symmetric fluctuations of η, around zero value, can not be detected by this method. The only influence related to this effect is a broadening of the peak, which is hard, if possible, to measure.

2. The NMR method treats the quadrupole term in the Hamiltonian as a small perturbation.

3. The NMR method can't detect internal structure of the NQR spectrum. Whereas, by using the ADNQR technique we can measure η for each and every point in the $YBCO_{6.675}$ spectrum. This may give us more data on the 30MHz peak, which is of great interest.

4. A major disadvantage of the NMR technique is its sensitivity. Adding the NMR field to a narrow NQR spectrum makes it broader, and in order to measure all the nuclei of the sample we must scan the spectrum. This means that in each measurement we detect only part of the nuclei. Since the ADNQR technique doesn't shift the system energy levels we can measure all the nuclei at the same time. This of course improves the sensitivity of the method.

5. The NMR technique uses a very strong magnetic field, that may change part of the sample properties, (electronic configuration for instance), which in turn change η. This problem doesn't exist in the ADNQR technique.

6. Since the result depends on η^4 for small η, the ADNQR method is not accurate for small values of η.

7. The ADNQR technique requires an oriented sample. This raises two difficulties. We must know the orientation quality to evaluate a numerical value for η, and we must know the direction of V_{zz} with respect to the orientation direction.

Appendix A

Spin $\frac{1}{2}$ in magnetic field

The aim of this appendix is to describe the motion of a spin in magnetic fields. In the quantum mechanical approach it means finding the wave function and calculating the observables expectation values.

A.1 Static homogenous magnetic field

We start by looking at the interaction of a spin with a static homogenous magnetic field $\mathbf{B_0} = (0, 0, B_0)$. We shall confine ourselves to spin $\frac{1}{2}$.

The nucleus possesses a total magnetic moment $\boldsymbol{\mu}$, which is related to its total angular momentum $\hat{I}$, by the scalar γ- the "gyromagnetic ratio". The relation is

$$\boldsymbol{\mu} = \gamma\hbar\hat{\mathbf{I}} \tag{A.1}$$

where

$$\hat{\mathbf{I}} = \left[\begin{pmatrix} 0 & \frac{1}{2} \\ \frac{1}{2} & 0 \end{pmatrix}, \begin{pmatrix} 0 & -i\frac{1}{2} \\ i\frac{1}{2} & 0 \end{pmatrix}, \begin{pmatrix} \frac{1}{2} & 0 \\ 0 & -\frac{1}{2} \end{pmatrix} \right] \tag{A.2}$$

(We work in the usual spin $\frac{1}{2}$ basis, $\langle\uparrow| \triangleq \begin{pmatrix} 1 & 0 \end{pmatrix}$ and $\langle\downarrow| \triangleq \begin{pmatrix} 0 & 1 \end{pmatrix}$).

The energy of a magnetic moment in a magnetic field is the scalar product of the two. The

Hamiltonian is therefore $\hat{H}_0 = -\boldsymbol{\mu} \cdot \mathbf{B_0}$, and by defining

$$\omega_0 \triangleq \gamma B_0 \tag{A.3}$$

it can be written as

$$\hat{H}_0 = -\frac{\hbar\omega_0}{2} \begin{pmatrix} 1 & 0 \\ 0 & -1 \end{pmatrix} \tag{A.4}$$

The wave function, Ψ, is a solution of Schrödinger's equation

$$i\hbar\frac{\partial}{\partial t}\Psi = \hat{H}_0\Psi \tag{A.5}$$

Since the Hamiltonian is time independent, and diagonal in our basis, the solution is straightforward

$$\Psi(t) = e^{i\frac{\omega_0\hbar}{2}\hat{I}_z t} \begin{pmatrix} \alpha \\ \beta \end{pmatrix} \triangleq \hat{U}_0^{NMR}(t) \begin{pmatrix} \alpha \\ \beta \end{pmatrix} \tag{A.6}$$

where α and β are time independent and are determined by initial condition. The normalized condition is $|\alpha|^2 + |\beta|^2 = 1$. $\hat{U}_0^{NMR}(t)$ is the time propagator of the system. We will see later that this propagator can be replaced by a transformation to a rotating frame with angular velocity $(0, 0, \omega_0)$, or in other words that this propagator actually rotates the spin around the z axis.

The expectation values of the nucleus magnetic moment are

$$\langle\mu_z\rangle_{(t)} = \langle\Psi(t)|\,\gamma\hbar\hat{I}_z\,|\Psi(t)\rangle = \frac{1}{2}\gamma\hbar\left(|\alpha|^2 - |\beta|^2\right) \tag{A.7}$$

$$\langle\mu_x\rangle_{(t)} = \langle\Psi(t)|\,\gamma\hbar\hat{I}_x\,|\Psi(t)\rangle = \gamma\hbar\,\mathrm{Re}(\alpha^*\beta e^{-i\omega_0 t}) \tag{A.8}$$

$$\langle\mu_y\rangle_{(t)} = \langle\Psi(t)|\,\gamma\hbar\hat{I}_y\,|\Psi(t)\rangle = \gamma\hbar\,\mathrm{Im}(\alpha^*\beta e^{-i\omega_0 t}) \tag{A.9}$$

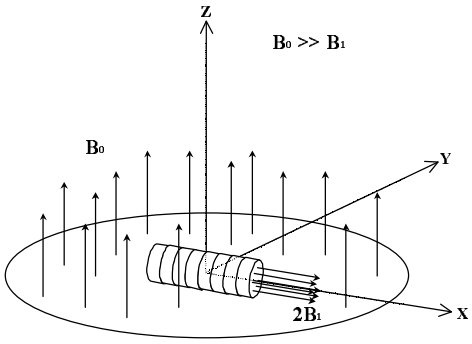

Figure A-1: Magnetic fields configuration in a basic NMR experiment. The coil produces a time dependent field - $2B_1$, perpendicular to a strong static field B_0.

A.2 Time periodic magnetic field

We now add a coil which is perpendicular to the homogenous field $\mathbf{B_0}$,as is illustrated in Fig A-1. If we apply an alternating voltage to the coil our spin will be subjected to a time periodic magnetic field. By defining the x and z direction as in the figure the total magnetic field is $\mathbf{B} = (2B_1\cos(\omega t), 0, B_0)$. The Hamiltonian is thus

$$\hat{H}(t) = \hat{H}_0 - 2\gamma\hbar B_1\cos(\omega t)\hat{I}_x \tag{A.10}$$

Equation A.10 can be written also as

$$\hat{H}(t) = \hat{H}_0 + \hat{H}(\omega) + \hat{H}(-\omega) \tag{A.11}$$

where we define

$$\hat{H}(\omega) \triangleq -\frac{1}{2}\gamma\hbar\begin{pmatrix} 0 & B_1e^{-i\omega t} \\ B_1e^{i\omega t} & 0 \end{pmatrix} \tag{A.12}$$

A.11 then means that the nucleus interacts with three fields. B_0 in the z direction, B_1 which rotates around the z direction clockwise and B_1 which rotates around the z direction counter-clockwise.

A.2.1 Transformation into a rotating frame

Unlike Eq A.4 this new Hamiltonian is time dependent and has off diagonal elements. Solving it will be much easier by transforming to a rotating frame. We make a rotation in real space around the z axis by the angle ωt . This rotated reference frame will be denoted by S' while the one in Fig A-1 is marked as S. Since the rotation is around the z axis the magnetic field vector (we treat both the rotation and the field classically) transforms in real space as

$$\mathbf{B}' = \begin{pmatrix} \cos(\omega t) & -\sin(\omega t) & 0 \\ \sin(\omega t) & \cos(\omega t) & 0 \\ 0 & 0 & 1 \end{pmatrix} \mathbf{B} \tag{A.13}$$

Transformations in the state space are of the form

$$\Psi' = e^{-i\omega t \hat{I}_z} \Psi \tag{A.14}$$

$$\hat{O}' = e^{-i\omega t \hat{I}_z} \hat{O} e^{i\omega t \hat{I}_z} \tag{A.15}$$

where $\hat{O}$ stands for an operator.

Using A.14, A.15 and A.13 allows us to write the Schrödinger equation in S' as $i\hbar \frac{\partial}{\partial t} \Psi'(t) = \hat{H}'(t)\Psi'(t)$ with

$$\hat{H}'(t) = \hat{H}'_0 + \hat{H}'(2\omega) + \hat{H}'(0) \tag{A.16}$$

where

$$\hat{H}'_0 \triangleq -\frac{1}{2}\gamma\hbar \begin{pmatrix} B_0 - \frac{\omega}{\gamma} & 0 \\ 0 & -B_0 + \frac{\omega}{\gamma} \end{pmatrix} \tag{A.17}$$

This result is interpreted as follows. The field which in the lab frame rotates around the z axis with frequency ω is now seen in the rotating frame with a double frequency, while the opposite one seems to be constant. This gives us the last two terms in A.16. The first term tells us that in the rotating frame the homogenous constant field has changed its value, though it is still

constant and in the z direction. We note here that the extra term $\frac{\omega}{\gamma}\hbar\hat{I}'_z$ in the Hamiltonian (A.17) will always appear in a time dependent rotation transformation. This is because S' is a non inertial frame. The same result is encountered in classical mechanics, where the extra term is the centripetal force.

Solution in the rotating frame

According to A.17 it seems worthwhile to choose a rotating frame with $\omega = \omega_0$, which is the resonance frequency of the unperturbed Hamiltonian (A.4). By defining first

$$\omega_1 = \gamma B_1 \tag{A.18}$$

The Hamiltonian in this rotating frame becomes

$$\hat{H}'(t) = -\frac{1}{2}\omega_1\hbar \begin{pmatrix} 0 & 1+e^{-i2\omega_0 t} \\ 1+e^{i2\omega_0 t} & 0 \end{pmatrix} \tag{A.19}$$

The interpretation of A.19 is that in this special rotating frame we have a two levels system with a degenerate energy $E = 0$. We also have two magnetic fields. One with an off resonance frequency, $2\omega_0$, and the other with a resonance frequency, zero. It is clear then that the off resonance field can be ignored since it induces rapid small oscillations between the states (see ref [14])[1], leading us to a non diagonal time independent Hamiltonian

$$\hat{H}' = -\frac{1}{2}\hbar\omega_1\hat{I}_x \tag{A.20}$$

According to A.14 and A.6

$$\Psi'(t=0) = \Psi(t=0) = \begin{pmatrix} \alpha \\ \beta \end{pmatrix} \tag{A.21}$$

[1] We call this type of omission the off resonance approximation.

And it evolves with time as

$$\Psi'(t) = e^{i\omega_1 \hat{I}'_x t} \begin{pmatrix} \alpha \\ \beta \end{pmatrix} \triangleq \hat{U}^{NMR}_{pulse}(t) \begin{pmatrix} \alpha \\ \beta \end{pmatrix} \tag{A.22}$$

The expectation values for the nucleus moment, in the rotating frame, are

$$\left\langle \mu'_z \right\rangle (t) = \left\langle \Psi'(t) \right| \gamma\hbar \hat{I}'_z \left| \Psi'(t) \right\rangle = \frac{1}{2}\gamma\hbar \left[\left(|\alpha|^2 - |\beta|^2 \right) \cos(\omega_1 t) - 2\sin(\omega_1 t)\,\mathrm{Im}(\alpha^*\beta) \right] \tag{A.23}$$

$$\left\langle \mu'_x \right\rangle (t) = \gamma\hbar\,\mathrm{Re}(\alpha^*\beta) \tag{A.24}$$

$$\left\langle \mu'_y \right\rangle (t) = \frac{1}{2}\gamma\hbar \left(|\alpha|^2 - |\beta|^2 \right) \sin(\omega_1 t) - \gamma\hbar i \cos(\omega_1 t)\,\mathrm{Im}(\alpha^*\beta) \tag{A.25}$$

These results seem to be quite messy, and instead of dealing with the general case we should look at a specific one. We assume that we start with a spin up, which means spin in the z direction. From A.21 this means $\beta = 0$. We also choose the alternating field in the coil to be a pulse of duration $t = \frac{\pi}{2\omega_1}$. In this case A.23-A.25 become

$$\begin{aligned} \left\langle \mu'_z \right\rangle_{(t=\frac{\pi}{2\omega_1})} &= 0 \\ \left\langle \mu'_x \right\rangle_{(t=\frac{\pi}{2\omega_1})} &= 0 \\ \left\langle \mu'_y \right\rangle_{(t=\frac{\pi}{2\omega_1})} &= \frac{1}{2}\gamma\hbar \end{aligned} \tag{A.26}$$

While according to A.7-A.9

$$\begin{aligned} \left\langle \mu'_z \right\rangle_{(t=0)} &= \left\langle \mu_z \right\rangle_{(t=0)} = \frac{1}{2}\gamma\hbar \\ \left\langle \mu'_x \right\rangle_{(t=0)} &= \left\langle \mu_x \right\rangle_{(t=0)} = 0 \\ \left\langle \mu'_y \right\rangle_{(t=0)} &= \left\langle \mu_y \right\rangle_{(t=0)} = 0 \end{aligned} \tag{A.27}$$

We thus see that the result of this so called $\frac{\pi}{2}$ pulse is to turn the spin, in the rotating frame,

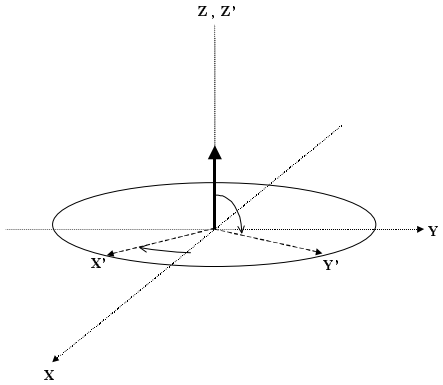

Figure A-2: The $\frac{\pi}{2}$ pulse rotates the spin from the z direction to y'. During the pulse time the frame S' rotates with angular velocity ω_0 around the z axis.

by 90 degrees, from the z' direction to the y' direction. This is illustrated in Fig A-2. The operator $\hat{U}^{NMR}_{pulse}(t)$,which was defined in Eq A.22, thus describes a rotation of a spin around the x' axis.

Expectation values in the laboratory frame

If we want to find the wave function in the S frame we simply insert Eq A.22 to Eq A.14 and get

$$\Psi(t) = \hat{U}^{NMR}_{\mathbf{0}}(t)\hat{U}^{NMR}_{pulse}(t) \begin{pmatrix} \alpha \\ \beta \end{pmatrix} \tag{A.28}$$

As can be seen from this result the transformation to the rotating frame (as it is defined in Eq A.14) is no more then the time propagator of the unperturbed Hamiltonian of Eq A.4. And as was mentioned before we can understand the propagator $\hat{U}^{NMR}_{\mathbf{0}}(t)$ as a transformation to a rotating frame.

A.2.2 An FID sequence

The free induction decay (FID) sequence is the simplest NMR experiment. It includes a pulse that rotates the spin by 90 degrees, and then a pause of time t in which only the field $\mathbf{B_0}$ exists.

As we've already seen the field $\mathbf{B_0}$ causes the spin to rotate around the z direction. The result of such an experiment, operating on the initial state $|\uparrow\rangle$, is therefore a spin that rotates in the xy plane around the z axis. From the previous results the wave function of such a sequence is given by

$$\Psi(t) = \hat{U}_{\mathbf{0}}^{NMR}(t)\hat{U}_{\mathbf{0}}^{NMR}(t_{\frac{\pi}{2}})\hat{U}_{pulse}^{NMR}(t_{\frac{\pi}{2}}) \begin{pmatrix} 1 \\ 0 \end{pmatrix}$$

A.3 Summary

- We have a two levels system of a spin $\frac{1}{2}$ in a constant magnetic field.
- We apply a time dependent perturbation by a sinusoidal pulse.
- In a specific rotating frame, where we can ignore the off resonance frequency, we got a time independent Hamiltonian.
- With a specific pulse length we can turn the spin from the up state to the xy plane, and then make it rotates in this plane.

Appendix B

A Special Case of NQR - $\eta = 0$

In this appendix we solve the NQR Hamiltonian for a specific simple case, $\eta = 0$. The importance of this case is in providing us an intuitive picture for the NQR case. We will compare this case with the one of NMR of spin $\frac{1}{2}$. At the end of the appendix we will provide an intuitive explanation why the signal intensity depends on the coil orientation, the result of chapter 4.

B.1 The Hamiltonian

The general Hamiltonian is given in Eq 4.15. In the case of zero η it is reduced to a diagonal form.

$$\hat{H}_q^{EFG} = \frac{\omega_0 \hbar}{2} \begin{pmatrix} 1 & 0 & 0 & 0 \\ 0 & -1 & 0 & 0 \\ 0 & 0 & -1 & 0 \\ 0 & 0 & 0 & 1 \end{pmatrix} \tag{B.1}$$

The transformation 4.16 is reduced to the identity operator, and the perturbation matrix gets the simple form

$$\begin{aligned}\hat{W}^{EFG}(t) &= 2\hbar\omega_1\cos(\omega t)\cos(\theta)\begin{pmatrix}\frac{3}{2}&0&0&0\\0&\frac{1}{2}&0&0\\0&0&-\frac{1}{2}&0\\0&0&0&-\frac{3}{2}\end{pmatrix}\\ &+2\hbar\omega_1\cos(\omega t)\sin(\theta)\begin{pmatrix}0&\frac{\sqrt{3}}{2}&0&0\\\frac{\sqrt{3}}{2}&0&1&0\\0&1&0&\frac{\sqrt{3}}{2}\\0&0&\frac{\sqrt{3}}{2}&0\end{pmatrix}\end{aligned} \tag{B.2}$$

where we chose to apply a pulse in the xz plane, $\phi = 0$. Since $\eta = 0$ we know that the problem is independent of ϕ. For the same reasons as in chapter 4 we omit the diagonal elements of the first term on the RHS of Eq B.2. The off resonance approximation allows us, as before, to ignore the 1's in the perturbation matrix and to obtain the total Hamiltonian

$$\hat{H}(t) = \frac{\omega_0\hbar}{2}\begin{pmatrix}1&0&0&0\\0&-1&0&0\\0&0&-1&0\\0&0&0&1\end{pmatrix} + \sqrt{3}\hbar\omega_1\cos(\omega t)\sin(\theta)\begin{pmatrix}0&1&0&0\\1&0&0&0\\0&0&0&1\\0&0&1&0\end{pmatrix} \tag{B.3}$$

The last result immediately explains why in the case of $\eta = 0$ and $\theta = 0$ the signal is zero. The perturbation in this case can not couple between the energy levels and it is effectively zero.

The wave function

Like before we seek a solution of the form

$$\Psi^{EFG}(t) = \begin{pmatrix}e^{-i\frac{\omega_0}{2}t}&0&0&0\\0&e^{i\frac{\omega_0}{2}t}&0&0\\0&0&e^{i\frac{\omega_0}{2}t}&0\\0&0&0&e^{-i\frac{\omega_0}{2}t}\end{pmatrix}\varphi(t) \triangleq \hat{U}_{\mathbf{0}}^{\eta=\mathbf{0}}(t)\varphi(t)$$

To find the time propagator during the pulse we use the result of chapter 4 with the corresponding values

$$D_0 = \frac{\sqrt{3}}{2} \qquad \lambda = 0 \qquad \Gamma = \sin(\theta) \qquad \epsilon = \frac{\sqrt{3}}{2}\omega_1 \sin(\theta)$$

to receive

$$\hat{U}^{\eta=0}_{pulse}(t) = \begin{pmatrix} e^{-i\sqrt{3}\omega_1 \sin(\theta)\hat{I}_x t_{\frac{\pi}{2}}} & \begin{pmatrix} 0 & 0 \\ 0 & 0 \end{pmatrix} \\ \begin{pmatrix} 0 & 0 \\ 0 & 0 \end{pmatrix} & e^{-i\sqrt{3}\omega_1 \sin(\theta)\hat{I}_x t_{\frac{\pi}{2}}} \end{pmatrix} \tag{B.4}$$

The wave function for an all spin echo sequence is therefore

$$\Psi^{EFG}_{echo}(t + 2t_{\frac{\pi}{2}} + \tau + t_{\frac{\pi}{2}}) = \hat{U}^{\eta=0}_0(t + 2t_{\frac{\pi}{2}})\hat{U}^{\eta=0}_{pulse}(2t_{\frac{\pi}{2}})\hat{U}^{\eta=0}_0(\tau + t_{\frac{\pi}{2}})\hat{U}^{\eta=0}_{pulse}(t_{\frac{\pi}{2}})\varphi(0) \tag{B.5}$$

B.2 Comparison with NMR of spin $\frac{1}{2}$

Comparison of the wave functions

For the sake of simplicity we shall compare the two cases for a simple FID sequence. The generalization to a full spin echo sequence is straightforward. We find it useful to introduce the following quantities:

$\begin{pmatrix} 0 & 0 \\ 0 & 0 \end{pmatrix} \triangleq \hat{O}$

$\varphi(0) \triangleq |0\rangle$ for spin $\frac{1}{2}$.

$\varphi(0) \triangleq \left| \begin{matrix} u \\ d \end{matrix} \right\rangle$ for spin $\frac{3}{2}$.

$\hat{I}_i (i = x, y, z)$ are the angular momentum operators for spin $\frac{1}{2}$.

$\hat{I}^A_i (i = x, y, z)$ are the angular momentum operators for spin $\frac{3}{2}$.

In appendix A we found that for the NMR case the wave function of such a sequence was

$$\Psi^{NMR}_{FID}(t + t_{\frac{\pi}{2}}) = e^{i\omega_0 \hat{I}_z \left(t + t_{\frac{\pi}{2}}\right)} e^{i\omega_1 \hat{I}_x t_{\frac{\pi}{2}}} |0\rangle \tag{B.6}$$

While for the NQR case with zero η the result can be written as

$$\Psi_{FID}^{\eta=0}(t+t_{\frac{\pi}{2}}) = \hat{U}_{\mathbf{0}}^{\eta=\mathbf{0}}(t+t_{\frac{\pi}{2}})\hat{U}_{pulse}^{\eta=\mathbf{0}}(t_{\frac{\pi}{2}}) \left| \begin{matrix} u \\ d \end{matrix} \right\rangle$$
$$\begin{pmatrix} e^{i(-\omega_0)\hat{I}_z\left(t+t_{\frac{\pi}{2}}\right)} & \hat{O} \\ \hat{O} & e^{i\omega_0\hat{I}_z\left(t+t_{\frac{\pi}{2}}\right)} \end{pmatrix} \begin{pmatrix} e^{-i\sqrt{3}\omega_1\sin(\theta)\hat{I}_x t_{\frac{\pi}{2}}} & \hat{O} \\ \hat{O} & e^{-i\sqrt{3}\omega_1\sin(\theta)\hat{I}_x t_{\frac{\pi}{2}}} \end{pmatrix} \left| \begin{matrix} u \\ d \end{matrix} \right\rangle$$

In a more convenient way we can rewrite the last result as

$$\Psi_{FID}^{\eta=0}(t+t_{\frac{\pi}{2}}) = \begin{pmatrix} e^{i(-\omega_0)\hat{I}_z\left(t+t_{\frac{\pi}{2}}\right)}e^{-i\sqrt{3}\omega_1\sin(\theta)\hat{I}_x t_{\frac{\pi}{2}}} & \hat{O} \\ \hat{O} & e^{i\omega_0\hat{I}_z\left(t+t_{\frac{\pi}{2}}\right)}e^{-i\sqrt{3}\omega_1\sin(\theta)\hat{I}_x t_{\frac{\pi}{2}}} \end{pmatrix} \left| \begin{matrix} u \\ d \end{matrix} \right\rangle \tag{B.7}$$

By comparing Eq B.6 with Eq B.7 we conclude that the wave function of the NQR case evolves with time as if it is composed of two uncoupled spins half. One behaves as a simple NMR of spin $\frac{1}{2}$ case (the down subspace), and the other acts as a NMR of spin $\frac{1}{2}$ case that rotates in the opposite direction with respect to the z axis.

Comparison of the expectation values

The last conclusion is for the wave function, but since the measured quantities are the observables we must compare them in order to receive the right intuitive analogy between the two cases. We start with the NMR case

$$\left\langle \hat{I}_z \right\rangle \propto \langle 0| e^{-i\omega_1\hat{I}_x t_{\frac{\pi}{2}}} e^{-i\omega_0\hat{I}_z\left(t+t_{\frac{\pi}{2}}\right)} \begin{pmatrix} \frac{1}{2} & 0 \\ 0 & -\frac{1}{2} \end{pmatrix} e^{i\omega_0\hat{I}_z\left(t+t_{\frac{\pi}{2}}\right)} e^{i\omega_1\hat{I}_x t_{\frac{\pi}{2}}} |0\rangle \tag{B.8}$$

$$\left\langle \hat{I}_x \right\rangle \propto \langle 0| e^{-i\omega_1\hat{I}_x t_{\frac{\pi}{2}}} e^{-i\omega_0\hat{I}_z\left(t+t_{\frac{\pi}{2}}\right)} \begin{pmatrix} 0 & \frac{1}{2} \\ \frac{1}{2} & 0 \end{pmatrix} e^{i\omega_0\hat{I}_z\left(t+t_{\frac{\pi}{2}}\right)} e^{i\omega_1\hat{I}_x t_{\frac{\pi}{2}}} |0\rangle \tag{B.9}$$

$$\left\langle \hat{I}_y \right\rangle \propto \langle 0|\, e^{-i\omega_1 \hat{I}_x t_{\frac{\pi}{2}}} e^{-i\omega_0 \hat{I}_z \left(t+t_{\frac{\pi}{2}}\right)} \begin{pmatrix} 0 & -i\frac{1}{2} \\ i\frac{1}{2} & 0 \end{pmatrix} e^{i\omega_0 \hat{I}_z \left(t+t_{\frac{\pi}{2}}\right)} e^{i\omega_1 \hat{I}_x t_{\frac{\pi}{2}}} |0\rangle \tag{B.10}$$

For the NQR case we have

$$\begin{aligned} \left\langle \hat{I}_z^4 \right\rangle \quad \propto \quad & \langle u, d| \begin{pmatrix} e^{i\sqrt{3}\omega_1 \sin(\theta) \hat{I}_x t_{\frac{\pi}{2}}} e^{-i(-\omega_0)\hat{I}_z \left(t+t_{\frac{\pi}{2}}\right)} & \hat{O} \\ \hat{O} & e^{i\sqrt{3}\omega_1 \sin(\theta) \hat{I}_x t_{\frac{\pi}{2}}} e^{-i\omega_0 \hat{I}_z \left(t+t_{\frac{\pi}{2}}\right)} \end{pmatrix} \\ & \times \begin{pmatrix} \frac{3}{2} & 0 & 0 & 0 \\ 0 & \frac{1}{2} & 0 & 0 \\ 0 & 0 & -\frac{1}{2} & 0 \\ 0 & 0 & 0 & -\frac{3}{2} \end{pmatrix} \times \\ & \begin{pmatrix} e^{i(-\omega_0)\hat{I}_z \left(t+t_{\frac{\pi}{2}}\right)} e^{-i\sqrt{3}\omega_1 \sin(\theta) \hat{I}_x t_{\frac{\pi}{2}}} & \hat{O} \\ \hat{O} & e^{i\omega_0 \hat{I}_z \left(t+t_{\frac{\pi}{2}}\right)} e^{-i\sqrt{3}\omega_1 \sin(\theta) \hat{I}_x t_{\frac{\pi}{2}}} \end{pmatrix} \left| \begin{matrix} u \\ d \end{matrix} \right\rangle \end{aligned} \tag{B.11}$$

Or in another way

$$\begin{aligned} \left\langle \hat{I}_z^4 \right\rangle \quad \propto \quad & \langle u|\, e^{i\sqrt{3}\omega_1 \sin(\theta) \hat{I}_x t_{\frac{\pi}{2}}} e^{-i(-\omega_0)\hat{I}_z \left(t+t_{\frac{\pi}{2}}\right)} \begin{pmatrix} \frac{3}{2} & 0 \\ 0 & \frac{1}{2} \end{pmatrix} e^{i(-\omega_0)\hat{I}_z \left(t+t_{\frac{\pi}{2}}\right)} e^{-i\sqrt{3}\omega_1 \sin(\theta) \hat{I}_x t_{\frac{\pi}{2}}} |u\rangle + \\ & \langle d|\, e^{i\sqrt{3}\omega_1 \sin(\theta) \hat{I}_x t_{\frac{\pi}{2}}} e^{-i\omega_0 \hat{I}_z \left(t+t_{\frac{\pi}{2}}\right)} \begin{pmatrix} -\frac{1}{2} & 0 \\ 0 & -\frac{3}{2} \end{pmatrix} e^{i\omega_0 \hat{I}_z \left(t+t_{\frac{\pi}{2}}\right)} e^{-i\sqrt{3}\omega_1 \sin(\theta) \hat{I}_x t_{\frac{\pi}{2}}} |d\rangle \end{aligned} \tag{B.12}$$

Using the fact that

$$\begin{aligned} \begin{pmatrix} \frac{3}{2} & 0 \\ 0 & \frac{1}{2} \end{pmatrix} &= \begin{pmatrix} \frac{1}{2} & 0 \\ 0 & -\frac{1}{2} \end{pmatrix} + \begin{pmatrix} 1 & 0 \\ 0 & 1 \end{pmatrix} \\ \begin{pmatrix} -\frac{1}{2} & 0 \\ 0 & -\frac{3}{2} \end{pmatrix} &= \begin{pmatrix} \frac{1}{2} & 0 \\ 0 & -\frac{1}{2} \end{pmatrix} - \begin{pmatrix} 1 & 0 \\ 0 & 1 \end{pmatrix} \end{aligned}$$

allows us to write Eq B.12 as

$$\left\langle \hat{I}_z^4 \right\rangle \propto 1 + \langle u| e^{i\sqrt{3}\omega_1 \sin(\theta)\hat{I}_x t_{\frac{\pi}{2}}} e^{-i(-\omega_0)\hat{I}_z\left(t+t_{\frac{\pi}{2}}\right)} \begin{pmatrix} \frac{1}{2} & 0 \\ 0 & -\frac{1}{2} \end{pmatrix} e^{i(-\omega_0)\hat{I}_z\left(t+t_{\frac{\pi}{2}}\right)} e^{-i\sqrt{3}\omega_1 \sin(\theta)\hat{I}_x t_{\frac{\pi}{2}}} |u\rangle$$
$$-1 + \langle d| e^{i\sqrt{3}\omega_1 \sin(\theta)\hat{I}_x t_{\frac{\pi}{2}}} e^{-i\omega_0\hat{I}_z\left(t+t_{\frac{\pi}{2}}\right)} \begin{pmatrix} \frac{1}{2} & 0 \\ 0 & -\frac{1}{2} \end{pmatrix} e^{i\omega_0\hat{I}_z\left(t+t_{\frac{\pi}{2}}\right)} e^{-i\sqrt{3}\omega_1 \sin(\theta)\hat{I}_x t_{\frac{\pi}{2}}} |d\rangle \quad \text{(B.13)}$$

Comparing Eq B.13 with Eq B.8 proves us that indeed the conclusion about the wave function is valid for $\left\langle \hat{I}_z^4 \right\rangle$ too. The NQR case can be divided into two NMR spin $\frac{1}{2}$ cases. The first case, the up subspace, behaves as a spin $\frac{1}{2}$ but with one difference: its average value, in the z direction, is shifted by one angular momentum unit. The second case, the down subspace, behaves as a spin $\frac{1}{2}$ with an average value of -1, and it rotates around the z axis with an opposite direction compared to the up subspace. For the y component we write $\hat{I}_y^4$ as

$$\hat{I}_y^4 = \begin{pmatrix} \begin{pmatrix} 0 & -i\frac{\sqrt{3}}{2} \\ i\frac{\sqrt{3}}{2} & 0 \end{pmatrix} & 0 \\ 0 & 0 \end{pmatrix} + \begin{pmatrix} 0 & 0 \\ 0 & \begin{pmatrix} 0 & -i\frac{\sqrt{3}}{2} \\ i\frac{\sqrt{3}}{2} & 0 \end{pmatrix} \end{pmatrix} + \begin{pmatrix} 0 & \begin{pmatrix} 0 & 0 \\ -i & 0 \end{pmatrix} \\ 0 & 0 \end{pmatrix} + \begin{pmatrix} 0 & 0 \\ \begin{pmatrix} 0 & i \\ 0 & 0 \end{pmatrix} & 0 \end{pmatrix} \quad \text{(B.14)}$$

The first two terms give us

$$\left\langle \hat{I}_y^4 \right\rangle \propto \langle u| e^{i\sqrt{3}\omega_1 \sin(\theta)\hat{I}_x t_{\frac{\pi}{2}}} e^{-i(-\omega_0)\hat{I}_z\left(t+t_{\frac{\pi}{2}}\right)} \begin{pmatrix} 0 & -i \\ i & 0 \end{pmatrix} e^{i(-\omega_0)\hat{I}_z\left(t+t_{\frac{\pi}{2}}\right)} e^{-i\sqrt{3}\omega_1 \sin(\theta)\hat{I}_x t_{\frac{\pi}{2}}} |u\rangle$$
$$+ \langle d| e^{i\sqrt{3}\omega_1 \sin(\theta)\hat{I}_x t_{\frac{\pi}{2}}} e^{-i\omega_0\hat{I}_z\left(t+t_{\frac{\pi}{2}}\right)} \begin{pmatrix} 0 & -i \\ i & 0 \end{pmatrix} e^{i\omega_0\hat{I}_z\left(t+t_{\frac{\pi}{2}}\right)} e^{-i\sqrt{3}\omega_1 \sin(\theta)\hat{I}_x t_{\frac{\pi}{2}}} |d\rangle \quad \text{(B.15)}$$

Eq B.15 relates to Eq B.10 as Eq B.13 relates to Eq B.8, and the analogy is therefore clear. The last two terms of the RHS of Eq B.14 are obviously off diagonal in the 4×4 matrix

$$\left[\hat{U}_{\mathbf{0}}^{\eta=0}(t+t_{\frac{\pi}{2}})\hat{U}_{pulse}^{\eta=0}(t_{\frac{\pi}{2}})\right]^{\dagger} \hat{I}_y^4 \left[\hat{U}_{\mathbf{0}}^{\eta=0}(t+t_{\frac{\pi}{2}})\hat{U}_{pulse}^{\eta=0}(t_{\frac{\pi}{2}})\right]$$

Which is the matrix that yields $\left\langle \hat{I}_y^4 \right\rangle$ before inserting the bra and ket $|0\rangle$ (like in B.11). In other words it means that these two terms are 4×4 matrices with zeros on their diagonal. Since $\varphi(0)$ is one of the eigenstates of $\hat{I}_z^4$ (Thermal equilibrium surely provides us the system in one of its eigenstates) we know that we will get zero when calculating the expectation value for these two matrices with $|0\rangle$. The conclusion is then that Eq B.15 is the right solution for $\left\langle \hat{I}_y^4 \right\rangle$, and again it describes the system as a motion of two independent spins $\frac{1}{2}$ in an NMR experiment. The calculation and conclusion for the x component are the same.

B.3 Total magnetization

From the last results we can obtain an explicit form of the magnetization for the $\eta = 0$ case. We use for $\varphi(0)$ the following wave functions

$$\begin{aligned}
\left\langle \begin{array}{cc|} u & d \end{array} \right. &= \begin{pmatrix} 1 & 0 & 0 & 0 \end{pmatrix} \Longrightarrow \langle u| = \begin{pmatrix} 1 & 0 \end{pmatrix}, \langle d| = \begin{pmatrix} 0 & 0 \end{pmatrix} \\
\left\langle \begin{array}{cc|} u & d \end{array} \right. &= \begin{pmatrix} 0 & 0 & 0 & 1 \end{pmatrix} \Longrightarrow \langle u| = \begin{pmatrix} 0 & 0 \end{pmatrix}, \langle d| = \begin{pmatrix} 0 & 1 \end{pmatrix} \\
\left\langle \begin{array}{cc|} u & d \end{array} \right. &= \begin{pmatrix} 0 & 1 & 0 & 0 \end{pmatrix} \Longrightarrow \langle u| = \begin{pmatrix} 0 & 1 \end{pmatrix}, \langle d| = \begin{pmatrix} 0 & 0 \end{pmatrix} \\
\left\langle \begin{array}{cc|} u & d \end{array} \right. &= \begin{pmatrix} 0 & 0 & 1 & 0 \end{pmatrix} \Longrightarrow \langle u| = \begin{pmatrix} 0 & 0 \end{pmatrix}, \langle d| = \begin{pmatrix} 1 & 0 \end{pmatrix}
\end{aligned} \tag{B.16}$$

Where the first two states have the same population as well as the last two. This means that for each up state there is always a down state, and vice versa. We would also like to define the operator

$$M \triangleq \begin{pmatrix} 0 & 1 \\ 1 & 0 \end{pmatrix} \tag{B.17}$$

which has the meaning of replacing the up and down states for the spin $\frac{1}{2}$ case. It is easy to show that M has the following properties

$$\begin{aligned}
M|u\rangle &= |d\rangle \quad , \quad M|d\rangle = |u\rangle \\
M\hat{I}_z M &= -\hat{I}_z \quad , \quad M\hat{I}_y M = -\hat{I}_y \quad , \quad M\hat{I}_x M = \hat{I}_x
\end{aligned}$$

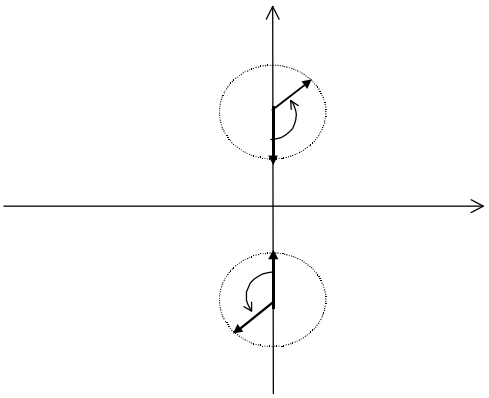

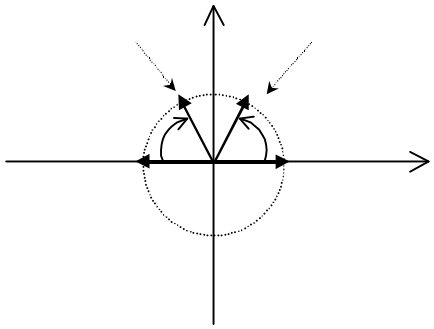

z xis wi cici wiscws bsc. Tls sii isscib i

Fig B-2.

Appendix C

Experimental Aspects of NMR/NQR

Until now we represented the entire NQR system as a simple coil that produce the time dependent magnetic field. As a concept it is enough, though practically the problem is much more complicated. The aim of this appendix is to describe basic NQR experiments and apparatus.

C.1 Hardware

Frequency range

We first have to know what is the relevant frequencies range. Using Eq A.3, with a magnetic field of the order of tesla, gives frequencies of tens and hundreds of MHz. In the NQR case the equation for the frequency is 4.12, which still gives us tens of MHz. Therefore the frequency range of our problem is the RF (radio frequency).

An important feature of RF electronics is the impedance matching, which means that whenever you cascade a unit into the circuit you have to tune its impedance to fit all the other circuit's units impedance. The basic idea behind the impedance tuning is that we are now dealing with a high time varying electro-magnetic field. The voltage and current are changing along the circuit, making the usual DC approach incorrect, and constrain us to treat the problem with the wave approach. With this approach the intersection of two different parts causes reflection

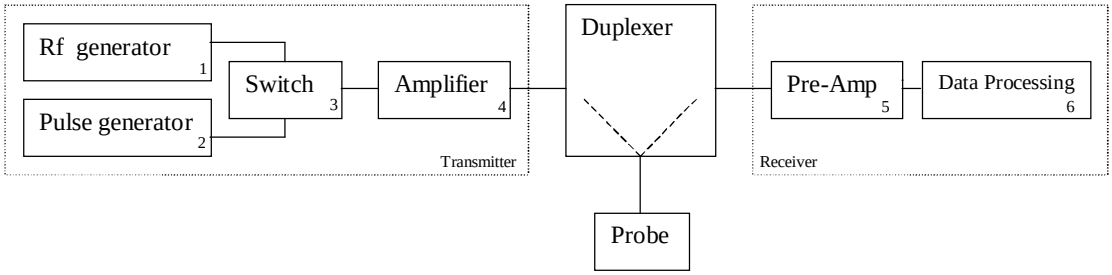

Figure C-1: Block diagram for the NQR system.

and transmission of the initial wave (like light between two media with refraction indices). To avoid reflection, which means losing power, we must have the same impedance (50Ω) for all the units in the circuit. (Which is the same as having equal index of refraction for the light case).

Block diagram

A schematic block diagram is shown in Fig C-1

Transmitter

The first three units function as a source for the sinusoidal pulses. A good RF generator should supply a continuous sinusoidal wave with high frequency and amplitude stability. The stability is less important when dealing with solid, or magnetic materials (YBCO), because in those materials the width of the signals, in the frequency domain, is much wider then in the liquid case. The pulse duration (see section C.3) is of the order of μsec, which restricts the switch and the pulse generator to have a raising time of about nsec.

A second important feature of the switch is its on-off ratio, which should be about four to six order of magnitude for the voltage attenuation. If in the off mode the leakage is too high the amplifying unit after the switch may cause a too strong induced field in the coil. This, in turn, rotates the spins back to the xy plane, against the natural relaxation process, and affects the relaxation rate. It is then clear that the leakage is more significant for a long T_1 relaxation experiment. In extreme cases, when T_1 is very long and the induced field is strong enough, the spins will be saturated and there will be no induced signal.

The amplifying unit receives an input of about a milliwatt. It's output power should be

between 100 to 1000 watts. It is therefore a high power RF pulse amplifier. To improve the power leakage between the pulses it may have gating stages included.

Receiver

The last two units function as the receiver stage of the system. The first one, the Pre-Amp, has a crucial role since it is the first gaining stage of the circuit. This stage amplifies the original signal to a level where it can be manipulated (modulated, filtered, multiplied, amplified etc.). Since the following gaining stages of the circuit will amplify the total output of the Pre-Amp (including the inevitable noise that the Pre-Amp himself creates) the most important feature of this unit is a low signal to noise ratio. This unit has to operate in the RF range, since no frequency modulation was yet done in the circuit till this stage. Since its input signal is of the order of microvolts it best be located close to the probe output. A band pass Pre-Amp has the advantage of reducing the noise level, but on the other hand it restricts the system to a defined frequencies range.

The last unit is responsible for data processing like frequency modulation (which removes the RF carrier frequency so that only the signal envelope remains), further gaining stage (of audio frequencies) and noises filtering (phase cycling).

Duplexer

This unit switches the connection of the probe between the transmitter and the receiver. There are a few difficulties this unit has to overcome:

1. The transmitter output voltage is hundreds of volts, while the receiver input voltage is microvolts. We thus must decouple the transmitter from the receiver.
2. We work with RF frequencies.
3. The switching time should be μsec.

One way of solving this problem is to use two orthogonal coils. One transmits the pulse to the sample and the other receives the signal. The main problem with this method is that it doesn't work in the NQR case, since the induced field is parallel to the transmitted one (see appendix B). For the NMR case it is indeed a useful method though not without difficulties.

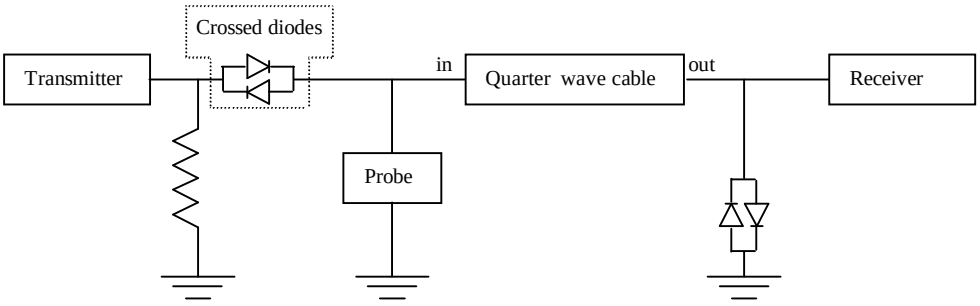

Figure C-2: Schematic description of a duplexer circuit.

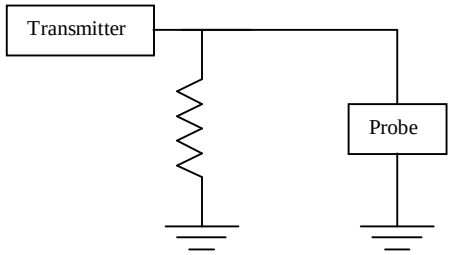

Figure C-3: The equivalent duplexer circuit during the RF pulse.

We now describe the duplexer we use in our laboratory. A schematic description is given in Fig C-2. A crossed diodes is a device that acts like a switch which is on for large signal with zero impedance, and off for low signal (~0.5 volt) with high impedance. When a high voltage RF pulse arrives from the left both crossed diodes behave like a zero impedance component, the output impedance of the quarter wave cable is thus zero, and the input impedance is infinity. This is because a quarter wave cable acts as transformer with the property that

$$Z_{in} Z_{out} = 250 \tag{C.1}$$

Where Z_{in} and Z_{out} are the input and output impedance of the cable. The circuit of Fig C-2 is thus reduced to the one of Fig C-3. We see then that this unit switches off the receiver from the transmitter when a high pulse is transmitted.

When the transmitter's pulse decreases below 0.5 volt the left crossed diode behaves as an infinite impedance component so the probe and the receiver are decoupled from the transmitter.

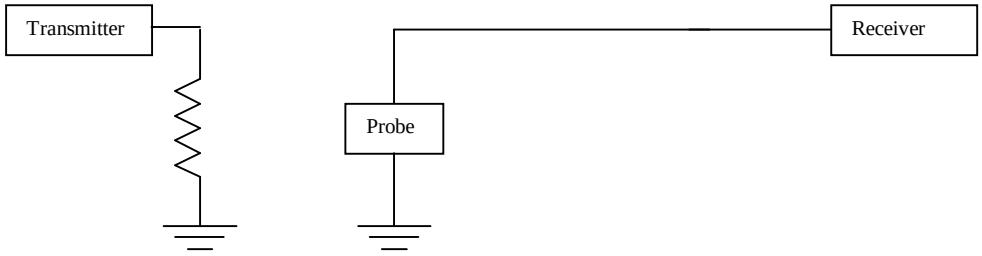

Figure C-4: The equivalent duplexer circuit after the RF pulse.

The right crossed diode also has infinite impedance since the probe's induced signal is very weak (less than one volt). Since Z_{in} is now 50Ω (the probe's impedance) Z_{out} is 50Ω too and we get the complete matched circuit of Fig C-4

The right crossed diode in Fig C-2 also guaranties that voltage higher than the diode's threshold voltage won't reach the Pre-Amp input, since for such a voltage the crossed diode is like a connection to the ground. Therefore it functions as a filter and guarding unit for the Pre-Amp, and since the induced signal's level is microvolts, the lower the threshold voltage the better it functions.

There are two major problems with this type of duplexer. One is the dependence of the quarter wave length on frequency. Changing the frequency will inevitably change the wave length and thus force us to change the cable length. It is therefore a bandpass device with an approximately 10% variation of the frequency. The second problem arises from the length of the cable at low frequencies (15 meters at 3MHz) which makes it an inefficient device for low frequencies.

Probe

The probe is the unit which contains the sample. As part of the RF circuit it must have a 50Ω impedance. Since we are interested in a specific frequency in each measurement it should include a narrow band pass filter inside. Furthermore, in solid and magnetic materials we have very broad lines (MHz), which we have to scan by changing the frequency for each measurement. We thus conclude that we need a tunable band pass filter with a constant 50Ω impedance. This is achieved by the probe.

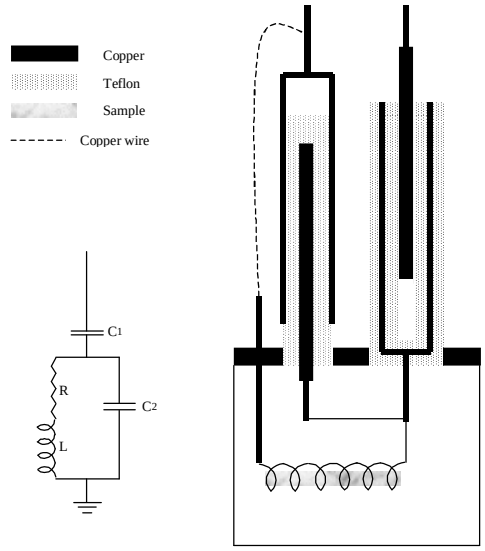

Figure C-5: The NMR/NQR probe.

Fig C-5 is a schematic description of the probe. A circuit equivalent to this unit appears in the low left corner of the figure. The impedance and resonance frequency of this circuit are given by the expressions [5].

$$Z = R\left(1 + \frac{C_2}{C_1}\right)^2 \tag{C.2}$$

$$\omega = \sqrt{\frac{1}{L(C_1 + C_2}} \tag{C.3}$$

In practice the matching of the impedance, and tuning of the resonance frequency, are done by changing the capacitors capacitance. This is done by pulling and pushing the external cylinder of the left capacitor, or the internal cylinder of the right capacitor.

In our laboratory we automatized this function. By connecting the external cylinder of left capacitor to a step motor we are now able to scan automatically a wide range of frequency ($\sim 3MHz$). This allows us to obtain a much more accurate and detailed spectrum.

The most important component of the probe is the coil because its features can be easily changed. According to Eq C.3 the probe's resonance frequency depends on the coil inductance,

so we have to choose a coil which agrees with the required frequency. Furthermore, the coil inductance and resistance affects the Q factor of the probe through the equation

$$Q = 2\pi\nu\frac{L}{R} \tag{C.4}$$

Where ν stands for frequency (MHz) and L and R are the inductance and resistance respectively. This in turn changes the signal to noise ratio, the width of the filter and its recovery time. The size of the coil should determine the size of the sample, so that the filling factor will be optimal. Since there are so many parameters and effects we usually use some rules of thumb to choose an appropriate coil

1. Its diameter should be the same as its length.
2. The space between the turns should be equal or less to the wire diameter.
3. The size of the sample should approximately determine the coil volume.
4. To change the coil resistance we change the wire diameter or material.

C.2 Basic pulse sequence

FID

This sequence is composed of one short pulse (of the order of μs), that rotates the spin from the z direction to the xy plane. It is therefore called a $\frac{\pi}{2}$ pulse. After the pulse ends the spin starts to rotate in the xy plane and by doing so induces a voltage in the coil. This induced voltage is the signal measured in the experiment. A detailed calculation for this sequence in the case of spin $\frac{1}{2}$ in a static magnetic field appears in appendix A.

Spin echo

The FID sequence has some practical disadvantages. The main problem is that the signal appears right after the pulse ends. Inevitably, there is a "dead time" after the pulse due to the relaxation process of the electronic circuits. In some materials the natural relaxation rates inside the sample are faster than the electronic relaxation, and this makes the signal detection

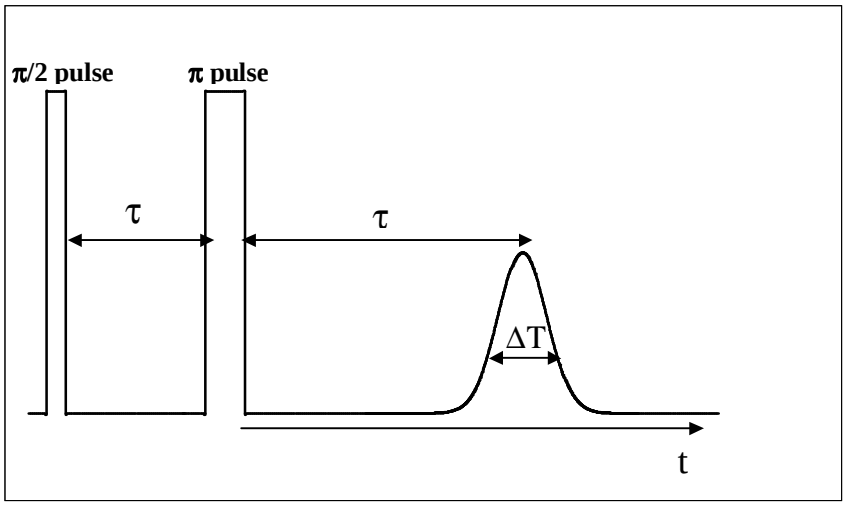

Figure C-6: Schematic description of a Spin Echo sequence. Two pulses followed by a gaussian shape echo.

impossible. The spin echo is a sequence of two pulses that enables us to detect the echo long after the electronic relaxation ends. The first pulse is a $\frac{\pi}{2}$ pulse. The second pulse is transmitted after a time τ, and is twice as long as the first pulse. This pulse rotates the spin by 180 degrees and is therefore called a π pulse. An illustration of such a sequence appears in Fig C-6. The two pulses appear as square wave forms, though in reality they consist of rapid sinusoidal oscillation (with frequency ω_0) inside the square shape envelopes. The gaussian form that appears after a time of 2τ is the induced signal.

To explain why this is the result of such a pulse sequence we choose to treat a spin $\frac{1}{2}$ in an external magnetic field in the z direction (NMR case). According to A.26 right after the $\frac{\pi}{2}$ pulse, in the x direction, the magnetization of the i'th spin is

$$\mathbf{M}_i(t_{\frac{\pi}{2}}) = \frac{1}{2}\gamma\hbar\,(0,1,0) \tag{C.5}$$

We then wait a time τ during which the spin precesses around the z direction with an angular

frequency

$$\omega = \gamma B_i \tag{C.6}$$

where B_i is the magnetic field (in the z direction) that the i'th spin feels. The magnetization after this time will be

$$\mathbf{M}_i(t_{\frac{\pi}{2}} + \tau) = \frac{1}{2}\gamma\hbar\left[\sin(\gamma B_i \tau), \cos(\gamma B_i \tau), 0\right] \tag{C.7}$$

We now apply the π pulse. It will rotate the spin, around the x direction, into the xy plane. Since this is a π pulse the spin will appear back in the xy plane, but phase shifted by $\pi + 2\gamma B_i \tau$. The magnetization is now

$$\mathbf{M}_i(t_{\frac{\pi}{2}} + \tau + t_\pi) = \frac{1}{2}\gamma\hbar\left[\sin(\pi - \gamma B_i \tau), \cos(\pi - \gamma B_i \tau), 0\right] \tag{C.8}$$

After the pulse ends the spin again precesses around the z axis and we get

$$\mathbf{M}_i(t_{\frac{\pi}{2}} + \tau + t_\pi + t) = \frac{1}{2}\gamma\hbar\left[\sin(\pi - \gamma B_i \tau + \gamma B_i t), \cos(\pi - \gamma B_i \tau + \gamma B_i t), 0\right] \tag{C.9}$$

We rewrite Eq C.9 to receive

$$\mathbf{M}_i(t_{\frac{\pi}{2}} + \tau + t_\pi + t) = \frac{1}{2}\gamma\hbar\left[\sin(\gamma\,(\tau - t)\,B_i), -\cos(\gamma\,(\tau - t)\,B_i), 0\right] \tag{C.10}$$

To get the total magnetization we have to sum over all the spins in the sample. Eq C.10 is the magnetization of the i'th spin which is subjected to the local static magnetic field B_i. In reality there is a spatial inhomogeneity of those local fields (in the z direction). This *time independent* inhomogeneity is due to imperfections in the sample, or in B_0 himself (see Fig A-1), that cause different internal fields in the sample. We will assume a normal distribution of those fields around a field value $B_0 = 0$ (this happens in the rotating frame). Under this assumption the

number of spins that feel the static magnetic field B is proportional to

$$\exp\left[-\left(\frac{B}{\delta B}\right)^2\right] dB \tag{C.11}$$

The total magnetization is thus

$$\mathbf{M}(t) \propto \int_{-\infty}^{\infty} dB \exp^{\left[-\left(\frac{B}{\delta B}\right)^2\right]} \left[\sin(\gamma\,(\tau - t)\,B), -\cos(\gamma\,(\tau - t)\,B), 0\right] \tag{C.12}$$

which yields

$$\mathbf{M}(t) \propto \exp\left[-\frac{\gamma^2\,(t-\tau)^2\,(\delta B)^2}{4}\right] \quad (\text{-}\widehat{y}) \tag{C.13}$$

We therefore have a gaussian centered at time τ after the second pulse with a width

$$\Delta T_{static} = \frac{1}{\gamma \delta B} \tag{C.14}$$

This result means that due to time independent spacial inhomogeneity of the field the spins loose their coherent phase. This effect is called dephasing. Its time scale is given by Eq C.14 and depends on the field inhomogeneity. An important feature of this process is its time independent reversibility. After the $\frac{\pi}{2}$ pulse it takes about ΔT time for the magnetization to dephase and disappear, but even if you wait a very long time ($\tau \gg \Delta T$) before you apply the π pulse the magnetization will be reconstructed with the same intensity. This time independent reversibility originates from the time independent field inhomogeneity.

C.3 Fluctuations processes

In the previous section we used a *time independent* inhomogeneous magnetic field in the z direction. We now elaborate the problem by inserting a time dependent field which fluctuates in the z direction. We will see that this field affects the system in two ways.

1. It causes the echo, in the time domain, to become wider. This effect is called motional narrowing. "Narrowing" refers to the echo width in the frequency domain, while "motional"

refers to movements inside liquid samples that cause the fluctuations.

2. Unlike the case of time independent field, in the fluctuating field the signal intensity does depend on time. The longer the waiting time the smaller the measured signal. Therefore it is advantageous to use as short a τ as possible.

Motional narrowing

In the static inhomogeneous field case the dephasing time scale was given by Eq C.14. An intuitive way to understand this result is to think of two spins subjected to two different magnetic field. According to Eq C.6 those two spins will gain angle (phase) between them while rotating in the xy plane. We denote this angle by $\Delta\Phi$. After a time t the value of this angle is

$$\Delta\Phi = \gamma\left(B_1 - B_2\right)t \tag{C.15}$$

We can define the out of phase state as $\Delta\Phi = 1$. This gives the dephasing time

$$t = \frac{1}{\gamma\left(B_1 - B_2\right)}$$

and the analogy between the last result and Eq C.14 is clear. Suppose now that these spins rotate a time t_1 and then ,simultaneously, the fields B_1 and B_2 change signs and rotate a time t_2 longer. The phase between the spins will now be

$$\Delta\Phi_{flip} = \gamma\left(B_1 - B_2\right)\left(t_1 - t_2\right) \tag{C.16}$$

while without the flip it would have been

$$\Delta\Phi_{without\ flip} = \gamma\left(B_1 - B_2\right)\left(t_1 + t_2\right) > \Delta\Phi_{flip}$$

We thus see that without fluctuations the spins lose phase faster than with fluctuation.

For large number of flips we solve the problem by introducing the parameter ν - the average

frequency of flipping. At each flip the phase can be changed by

$$\pm\gamma\left(B_1 - B_2\right)\frac{1}{\nu} \tag{C.17}$$

After a time $t = \frac{n}{\nu}$ the deviation from the average, which is zero phase difference, will be

$$\Delta\Phi = \sqrt{n}\gamma\left(B_1 - B_2\right)\frac{1}{\nu} = \gamma\left(B_1 - B_2\right)\sqrt{\frac{t}{\nu}} \tag{C.18}$$

Choosing a phase difference of 1 as the out of phase state we obtain a relation between the dynamic dephasing time and the static dephasing time

$$\Delta T_{dynamic} = \Delta T_{static} \times \left(\nu \Delta T_{static}\right) \tag{C.19}$$

In the limit $\nu\Delta T_{static} \gg 1$, which means rapid fluctuations compared to the spins precession rate (or in other words, large number of fluctuations during the time the echo is being built) we get an increase in the dephasing time, which is the motional narrowing effect.

Since the dephasing time is related to the field distribution by a Fourier transform we conclude that on a time scale of $\Delta T_{dynamic}$ the dynamic field distribution can be averaged to a static field distribution which is narrower than the original time independent field distribution by the factor $\frac{\gamma\delta B}{\nu}$. We can therefore replace Eq C.11 with the following distribution (in the rotating frame)

$$\frac{\gamma\delta B}{\nu}\exp\left[-\left(\frac{B}{\frac{\gamma\delta B^2}{\nu}}\right)^2\right]dB \tag{C.20}$$

T2 measurements

As was mentioned before we, expect the fluctuating case to be irreversible in time. In the static case we assumed that each spin rotates with a constant angular velocity, and *only* the π pulse reversed this angular velocity *once*, as can be seen in Eq C.9. Since the fluctuations cause reversion many times, we conclude that the treatment of the attenuation effects should be similar to Eq C.9. A detailed calculation can be found in ref [11], which yields a result of the form

$$\mathbf{M}_i(t=\tau) = \frac{1}{2}\gamma\hbar\left[0, -\left(1-\frac{\tau}{T_2}\right), 0\right] \tag{C.21}$$

Comparing Eq C.21 with Eq C.10 for $t=\tau$ shows us how the time irreversibility attenuates the signal from the value $-\frac{1}{2}\gamma\hbar$ to $-\frac{1}{2}\gamma\hbar\left(1-\frac{\tau}{T_2}\right)$. The total magnetization means integration of Eq C.21 with the field distribution of Eq C.20. This leads to

$$\mathbf{M}(t) \propto \left(\frac{\gamma\Delta B}{\nu}\right)^2\left(1-\frac{t}{T_2}\right)\exp\left[-\frac{\gamma^2(t-\tau)^2\left(\frac{\gamma\Delta B^2}{\nu}\right)^2}{4}\right] \quad (\text{-}\widehat{y}) \tag{C.22}$$

The experimental technique for measuring T_2 is to repeat the spin echo experiment with a different τ in each case, and measure the signal intensity as a function of τ. The slope of the resulting graph gives us the desired T_2.

T1 measurement

In the previous case we found the effect of the z component of the fluctuating field on the signal intensity. Although the magnetization component in the xy plane remains the same for each spin the total magnetization does decrease due to dephasing among the spins. But what about the fluctuations in the x and y direction? They will cause the spins in the xy plane to rotate in the yz and xz planes. Those spins gain a z component which means that they change their energy (due to the static field in the z direction). We thus see that the x and y components of the fluctuating field are responsible for the thermal equilibrium process. Unlike the z component process, this one causes the attenuation of the signal due to a decrease in the x and y components of the magnetization of *each* spin. We can characterize this relaxation process as

$$\mathbf{M}(t) = \mathbf{M_0}\exp\left(-\frac{t}{T_1}\right) \tag{4.28}$$

Where T_1 is the time scale for the relaxation. A pulse sequence to measure this time is shown in Fig C-7. In the beginning all the spins are in the same state - $|\uparrow\rangle$. The comb of the short

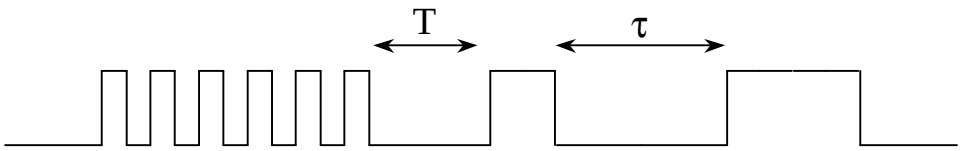

Figure C-7: A schematic pulse sequence for measuring T_1.

pulses causes them to lose their coherent state by the dephasing process, and reach a new state with no net magnetization in the z direction. This can be understood by thinking of the series of pulses as a continuous pulse that induces transitions between the energy levels. For a strong enough pulse the new state will have the same population for all the energy states, which means no magnetization in the external field direction (ref [18] section 1.3). This means that after the comb ends the only spins that can be manipulated are those that flipped back to the z direction and returned to the same quantum state - $|\uparrow\rangle$. The amount of those spins is proportional to $exp\left(-\frac{T}{T_1}\right)$, and since after the time T we apply a usual spin echo sequence, we expect to receive an echo which its intensity is proportional to $exp\left(-\frac{T}{T_1}\right)$. By repeating this sequence with different T's we can deduce the value of T_1.

Bibliography

[1] A.Abragam, *Principles of Nuclear Magnetism.* Oxford Science Publications.

[2] F.W.Carlson, V.J.Emery, S.A.Kivelson and D.Orgad, *Cond-mat/0206217.*

[3] M.H.Choen and F.Reif. *solid state physics (5)* (1957).

[4] M.Francois, A.Junod and K.Yvon, *Solid State Communications,* **66**, 1117 (1988).

[5] Eiichi Fukushima and Stephen B.W. Roeder. *Experimental pulse NMR, A Nuts And Bolts Approach.* Addison-Weslet Publishing, 1994.

[6] B.Grevin, Y.Bertheir and G.Collin, *Physical Review Letters,* **85**, 1310 (2000).

[7] T.P.Das and E.L.Hahn. *Nuclear Quadrupole Resonance Spectroscopy.* Academic Press Publisher, 1958.

[8] Katsurou Hanzawa, Fujihiko Komatsu and Kei Yosida, *Journal of the Physical Society of Japan,* **59**, 3345 (1990).

[9] J.D.Jorgensen, B.W.Veal, A.P.Paulikas, L.J.Nowicki, G.W.Crabtree, H.Claus and W.K.Kwok, *Physical review B,* **41**, 1863 (1990).

[10] A.Keren, P.Mendels, M.Horvatic, F.Ferrer, Y.J.Uemura, M.Mekata and T.Asano, *Physical review B,* **57**, 10745 (1998).

[11] A.Keren and Ophir M.Auslaender, *Physical review B,* **60**, 9279 (1999).

[12] M.Mali, D.Brinkmann, L.Pauli, J.Roos and H.Zimmerman, *Physics Letters A,* **124**, 112 (1987).

[13] P.Mendels and H.Alloul, *Physica C*, **156**, 355 (1988).

[14] Harold J.Metcalf, Peter van der Straten. *Laser Cooling and Trapping,* page 6. Springer.

[15] C.H.Pennington, D.J.Duand, D.B.Zax, C.P.Slichter, J.P.Rice and D.M.Ginsberg, *Physical review B*, **37**, 7944 (1988).

[16] R.V.Pound, *Physical Review,* **79**, 685 (1950).

[17] Tadashi Shimizu, Hiroshi Yasuoka, Takashi Imai, Toshinobu Tsuda, Toshiro Takabatake, Yasuhiro Nakazawa and Masayasu Ishikawa, *Journal of the Physical Society of Japan,* **57**, 2494 (1988).

[18] C.P.Slichter. *Principles of Magnetic Resonance*, Third edition. Springer-Verlag, 1990.

[19] C.C.Tannoudji, B.Diu and F.Laloë, *Quantum Mechanins.* page 1048.

[20] J.M.Tranquada *et al., Nature* **375,** 561 (1995).

[21] Alexander J.Vega, William E.Farneth, Eugene M.McCarron and Rajendra K.Bordia, *Physical review B*, **39**, 2322 (1989).

[22] W.W.Warren, Jr., R.E.Walstedt, G.F.Brennert, R.J.Cava, B.Batlogg and L.W.Rupp *Physical review B*, **39**, 831 (1989).

[23] Hiroshi Yasuoka, Tadashi Shimizu, Yutaka Ueda and Koji Kosuge, *Journal of the Physical Society of Japan,* **57**, 2659 (1988).

[24] J.Zaanen and O.Gunnarsson, *Physical review B,* **40,** 7391 (1989).

[25] F.C.Zhang and T.M.Rice, *Physical review B,* **37,** 3759 (1988).

פיתוח טכניקה המבוססת על קוודרופול גרעיני למדידת אי-הומוגניות של מטענים, ויישומה ל- YBCO

שחר לוי

פיתוח טכניקה המבוססת על קוודרופול גרעיני למדידת אי-הומוגניות של מטענים, ויישומה ל- YBCO

חיבור על מחקר

לשם מילוי חלקי של הדרישות לקבלת התואר מגיסטר למדעים בפיסיקה

שחר לוי

הוגש לסנט הטכניון - מכון טכנולוגי לישראל
סיון תשס"ג חיפה יוני 2003

המחקר נעשה בהנחיית פרופ' עמית קרן בפקולטה לפיסיקה בטכניון.

אני מודה לעמית קרן על הנחייתו המעולה. על התמיכה והעידוד שהעניק לי במשך תקופה ארוכה זאת, ועל מאמציו להעניק לי ביטחון וניסיון להמשך דרכי באשר היא.

אני מודה לפרופ' אמיל פולטורק על התמיכה הרבה שנתן לי במשך כל עבודת המחקר. על כך שבדרכו המיוחדת עודד אותי, גם בלי משים. ועל שלימד אותי פיסיקה ניסיונית מהי.

תודה מקרב לב לטכנאי המעבדה - גלינה בזליצקי, מרדכי אילון, שמואל הוידה וד"ר לאוניד יומין על העזרה הרבה שניתנה, ותמיד בשמחה.

תודה לכל חבריי בקבוצות המחקר למגנטיות ועל מוליכות- אווה, רינת, אורן, אושרי, אריאל, ליאור ומני על אוירת עבודה נפלאה.

ואחרון אחרון חביב- תודה חמה לעמית קניגל על העזרה הרבה בתחום המקצועי, והתמיכה בתחום האישי.

אני מודה לטכניון על התמיכה הכספית הנדיבה בהשתלמותי.

להוריי, דבורה ונחום, על תמיכה ואהבה אינסופית

תוכן עניינים

תקציר **1**

רשימת סמלים **3**

1. מבוא **4**

2. תוצאות עיקריות **10**
2.1 תיאוריה..... 10
2.2 אוריינטציה..... 12
2.3 סחיפת תדר..... 12
2.4 תוצאות ניסיוניות..... 14

3. מסקנות עיקריות **16**

4. תהודה קוודרופולית גרעינית **17**
4.1 אינטרקציה קוודרופולית- טיפול קלסי..... 17
4.2 גישה קוונטית..... 19
4.2.1 אינטרקציה עם שדה מגנטי חיצוני תלוי בזמן..... 22
4.3 מגנטיזציה בניסוי הד ספיני..... 27
4.4 סיכום..... 30

5. YBCO - מבנה ותכונות **32**

6. הכנה ואיפיון דגמים **36**
6.1 הכנה..... 36
6.2 שיטת איפיון, עקיפת קרני רנטגן..... 37
6.2.1 שיקולים מעשיים עבור ניסויי קרני רנטגן..... 41
6.3 סיכום..... 41

7. התאמה לנתונים **42**
7.1 אפקטים של התרחבות..... 42
7.2 אורינטציה של טנסור גרדיינט השדה החשמלי..... 44
7.2.1 תיקון של המשוואה..... 45

8. יתרונות וחסרונות **47**

A ספין חצי בשדה מגנטי **49**

B מקרה מיוחד של תהודה קוודרופולית גרעינית- $\eta=0$ **57**

C היבטים ניסיוניים של תהודה מגנטית/קוודרופולית גרעינית **66**

ביבליוגרפיה **80**

רשימת ציורים

1.1 Tc/Tc^{max} ו Tg/Tc^{max} כפונקציה של $\Delta p_m=p_m-p_m^{max}$. Tc^{max} היא הטמפ' הקריטית הגובהה ביותר שניתנת להשגה..... 5

1.2 אינטרקציית הקוודרופול החשמלית גורמת לאנרגיות שונות לאורינטציות שונות של הגרעין 6

1.3 תצורה בסיסית של תהודה קוודרופולית גרעינית התלויה בזוית (תקגת"ז) .דגם בצורת גליל מוכנס לתוך סליל. הזוית ביניהם, כפי שמתואר בשירטוט, ניתנת לשינוי..... 8

1.4 צורת הדגם היא גלילית. הכיוון המועדף מסומן בקו..... 9

2.1 עוצמה כתלות בזוית עבור ערכים שונים של סימטריה בניסוי תקגת"ז. תוצאות תאורטיות..... 11

2.2 יחס העוצמות עבור זוית 0 ו 90 מעלות כתלות בסימטריה. תוצאה תאורטית..... 12

2.3 ספקטרום התק"ג של הדגמים אותם מדדנו ב 100 K..... 13

2.4 תוצאה ניסיונית של תקגת"ז עבור $YBCO_7$ בתדר 31.15 מגה הרץ..... 14

2.5 תוצאה ניסיונית של תקגת"ז עבור $YBCO_{6.675}$ בתדר 27.501 מגה הרץ, ו $YBCO_7$ בתדר 30.53 מגה הרץ (כתף). התוצאה עבור השיא המרכזי של $YBCO_7$ זהה לזאת המופיעה בציור 2.4..... 15

4.1 משפט ויגנר אקרט מקשר בין ההצגות של בסיס המקום והתנע הזויתי ע"י קבוע..... 21

4.2 תאור סכמטי של רצף הד ספיני. לפרטים נוספים ראה נספח ג'..... 27

4.3 עוצמת ההד, עבור שידור במישור xy ,כתלות באורך הפולס. הערך האופטימלי נקבע בהתאם למקסימום הראשון..... 31

5.1 YBCO מבנה וסימונים..... 33

5.2 קבועי השריג של YBCO כפונקציה של החימצון בטמפ' חדר [10]..... 34

5.3 דיאגרמת פאזות של YBCO..... 35

6.1 התאבכות ע"י החזרה משני מישורים מקבילים. כאשר הפרש הדרכים האופטיות הוא כפולה של אורך גל מתקיים תנאי בראג..... 37

6.2 תוצאות עקיפת קרני רנטגן עבור $YBCO_7$. דגמים אלו הוכנו ע"י ניעור. גרף תחתון, דגם ללא כיוון מועדף. גרף אמצעי ועליון עם כיוון מועדף..... 38

6.3 כל גרגיר באבקה הוא שריג מושלם שמיוצג בשירטוט ע"י תשעה תאי יחידה צמודים. מישוריי 001 מסומנים באפור, ומקבילים בכל הדגם. כיוון מישורים אלו מסומן בקו על הדגם, כפי שמוצג באיור הימני..... 39

6.4 תוצאות עקיפת קרני רנטגן עבור $YBCO_7$. דגמים אלו הוכנו ללא ניעור..... 40

6.5 תוצאות עקיפת קרני רנטגן עבור $YBCO_{6.675}$. דגמים אלו הוכנו ללא ניעור..... 40

7.1 תוצאות ניסיוניות ותאורטיות עבור השיא של $YBCO_7$. הקו מתאר את ההתאמה הטובה ביותר, כולל השפעה של התרחבות הקו (ראה טקסט). תדר השידור הוא 31.15 מגה הרץ..... 43

7.2 תוצאות ניסיוניות ותאורטיות עבור הכתף של $YBCO_7$. הקו מתאר את ההתאמה הטובה ביותר, כולל השפעה של התרחבות הקו (ראה טקסט). תדר השידור הוא 30.53 מגה הרץ..... 44

7.3 תוצאות ניסיוניות ותאורטיות עבור $YBCO_{6.675}$. הקו מתאר את ההתאמה הטובה ביותר כולל השפעה של התרחבות הקו (ראה טקסט). תדר השידור הוא 27.501 מגה הרץ..... 45

7.4 אורינטצית הסליל עבור אורינטציות שונות של טנסור הגרדיינט החשמלי..... 46

A.1 שדות מגנטיים בניסוי בסיסי של תהודה גרעינית מגנטית. הסליל מייצר שדה מגנטי תלוי בזמן בניצב לכיוון השדה המגנטי החזק B_o..... 51

A.2 פולס 90 מעלות מסובב את הספין מכיוון z לכיוון y' . במשך שידור הפולס מערכת S' מסתובבת במהירות זוויתית ωo סביב ציר z..... 55

B.1 התפתחות ספין עבור תת מרחב עליון ותחתון בזמן פולס 90 מעלות..... 65
B.2| התפתחות ספין עבור תת מרחב עליון ותחתון לאחר פולס 90 מעלות..... 65
C.1 דיאגרמת בלוקים עבור מערכת תהודה קוודרופולית גרעינית..... 67
C.2 תאור סכימטי של מעגל duplexer..... 69
C.3 מעגל duplexer השקול בזמן שידור פולס..... 69
C.4 מעגל duplexer השקול לאחר שידור פולס..... 70
C.5 ה"ראש" של מערכת תהודה מגנטית/קוודרופטלית גרעינית..... 71
C.6 תאור סכימטי של רצף הד ספיני. שני פולסים מלווים בהד בעל צורה גאוסייאנית..... 73
C.7 תאור סכימטי של רצף פולסים למדידת T_1 79

תקציר

תופעת העל מוליכות בטמפרטורה גבוהה (~100K) נתגלתה בשנת 1986. עד היום, למרות המאמצים הרבים המושקעים בהבנתה, היא עדיין בעיה לא פתורה המהווה אתגר מרכזי בפיסיקה של מצב מוצק.

נוכחותם של מישורי Cu^{+2} בכל העל מוליכים בטמפ' גבוהות (Cuprates) מהווה רמז לחשיבותם בתהליך העל מוליכות. ואכן, מרבית התאוריות קושרות את התופעה הנ"ל לתכונות האופיניות למבנה הפנימי של מישורים אלו. כתוצאה מהמבנה הגבישי של ה-Cuprates ייתכנו שני סוגי יוניי נחושת במישורים הנ"ל, Cu^{+2} בעלי ספין חצי, ו Cu^{+3} אליהם ניתן להתייחס כחסרי ספין. השינוי בערכיות החשמלית נגרם כתוצאה משינוי כמות החמצן בחומר בתהליך הנקרא סימום. עובדה ניסיונית היא שבכל העל מוליכים הסימום משפיע באופן ניכר על תכונות העל מוליכות של החומר. ממצא זה, הקושר בין תופעת העל מוליכות לתכונות המגנטיות והחשמליות של המישורים, מהווה בסיס לתאוריות רבות באשר למנגנון המיקרוסקופי של התופעה. במצב של תת סימום כל יוניי הנחושת הם בעלי ספין. סימום המערכת גורם להופעת יוניי Cu^{+3} חסריי ספין (חורים). קיימות עדויות ניסיוניות, ותוצאות תיאורטיות, לכך שחורים נוטים להתאגד במבנים כדוגמת טיפות שמן במים, כלומר נוצרות שתי פאזות. ייתר על כן, בניסויים בפיזור ניטרונים גילו כי בחלק מהמקרים שתי הפאזות מסתדרות במבנה מחזורי. תוצאות אלו הובילו לפיתוח תיאורית הפסים (stripes), שבבסיסה הטיעון שהמבנה החד ממדי הוא חלק ממנגנון העל מוליכות, כלומר שקיום פסים הוא הכרחי לעל מוליכות. ככל שיהיו יותר חורים, הגדלת הסימום, יוצרו יותר פסים והעל מוליכות "תשתפר" (טמפ' המעבר לפאזה העל מוליכה תיגדל). מנגד, קיימות תיאוריות הטוענות שקיום מבנה מוגדר של הפאזה העשירה בחורים אינו הכרחי לעל מוליכות. היכולת למדוד את מבנה המטענים המישורים, ובייחוד את ההומוגניות שלהם, כתלות בסימום היא לפיכך בעלת חשיבות רבה להבנת מנגנון העל מוליכות.

קיימות מספר דרכים לכך לקביעת הומוגניות המטענים במישור:

1. μSR - טכניקה זאת מבוססת על מדידת השדה המגנטי בתוך החומר באופן מקומי. עבור סימום נמוך מאד החומר הוא אנטיפרומגנט, זהו מצב בו השדות המגנטיים המקומיים הם חזקים . עם העלאת הסימום הפאזה האנטיפרומגנטית נחלשת ומופיעים אזורים מגנטיים קטנים בתוך סביבה לא מגנטית (זכוכית ספינית). בעזרת טכניקה זאת ניתן למדוד את גודלם וחוזקם של האזורים הנ"ל, וזוהי אחת העדויות הניסיוניות לקיומן של אזורים עשירים ועניים בחורים. חסרונה של השיטה נובע מרגישותה. עם הגדלת הסימום האזורים המגנטיים קטנים ונחלשים עד שלב שבו לא ניתם למדודם בטכניקה זאת. שיטה זאת מוגבלת לפיכך לרמת סימום נמוכה. לא ניתן להסיק ממנה האם הגדלה נוספת של הסימום גורמת להעלמות מוחלטת של האזורים המגנטיים (מצב הומוגני בו שתי הפאזות התערבבו), או לקיומם במבנים קטנים מאד (פאזה לא הומוגנית). לפיכך לא ניתן להעיד באמצעותה על חשיבות המבנה הלא הומוגני לעל מוליכות ברמות סימום גבוהות.
2. STM- בטכניקה זאת סורקים את פני החומר ברמה המיקרוסקופית ומודדים את המבנה האלקטרוני שלו. מאחר והמצב העל מוליך קשור למבנה האלקטרוני ניתן ללמוד בשיטה זאת על התפלגות הפאזה העל מוליכה בחומר. ואכן, גם שיטה זאת מראה על התגבשות החומר במבנים לא הומוגניים התלויים בסימום. חסרונה של השיטה נעוץ בכך שהיא מודדת רק את פני החומר.
3. פיזור ניטרונים- מאחר ופיזור ניטרונים קשור לספין היונים ניתן בשיטה זאת ללמוד על מבנה מחזורי בחומר. חסרונה נעוץ בכך שהיא דורשת דגם גדול, ומחייבת מבנה מחזורי. כאמור, שיטה זאת סיפקה את העדות הראשונה לקיומם של מבנים מחזוריים במישורים (פסים). עד היום לא הצליחו למדוד בטכניקה זאת קיומם של פסים ב YBCO (סוג של על מוליך ממשפחת ה- Cuprates). עובדה אחרונה זאת מערערת את חשיבות הפסים כמנגנון מרכזי לעל מוליכות.

מכלול הגורמים הנ"ל מקשה על מציאת תשובה לשאלה: **<u>כיצד משתנה הומוגניות המטענים במישורים כתלות בסימום, החל ממצב של חוסר סימום ועד לסימום מלא ?</u>** אם ניתן יהיה למצוא עדות ניסיונית לכך

שהגדלת הסימום לא מגדילה את הומוגניות המטענים במישורים תיהיה בכך מישום ראיה כנגד תאורית הפסים.

בניסיון להתמודד עם בעיה זאת בדקנו אפשרות למדוד את אי הומוגניות המטענים בשיטה שונה, NQR (תהודה קוודרופולית גרעינית). שיטה זאת משמשת מזה זמן רב ככלי מרכזי בחקר העל מוליכות, והיא קשורה קשר ישיר לאי הומוגניות של מטענים. אלא שאליה וקוץ בה, בצורות המדידה הנהוגות בשיטה זאת עד היום קיים קושי רב מאד במדידת פרמטר האי הומוגניות בחומרים אלו. הבעיה נעוצה במורכבות ספקטרום ה-NQR של חומרים אלו (שהוא נושא למחקר בפני עצמו). התוצאות היחידות שהתקבלו בשיטה זאת עד היום הן עבור סימום מלא או חוסר סימום מוחלט, מקרים בהם הספקטרום פשוט ביותר.

במסגרת עבודה זאת פיתחנו טכניקה חדשה המשתמשת ב NQR. טכניקה זאת מודדת באופן ישיר את אי הומוגניות המטענים, ומסוגלת להתמודדת עם מורכבות הספקטרום כתלות בסימום. עבודתנו התרכזה לפיכך בשני רובדים.
הרובד הראשון מתיחס לפיתוח הטכניקה ובדיקת תקיפותה באופן ניסיוני. כלומר חישוב התוצאות הצפויות בניסוי ובדיקה ניסיונית. פיתרון מתמטי מדויק המתאר את הצפי התאורטי של הניסוי אותו ביצענו (הד ספיני עבור תהודה קוודרופולית גרעינית תלוית זוית) מופיע בפרק 4. בנספחים 1 ו 2 מופיע תאור מתמטי מפורט של טכניקת NMR (תהודה מגנטית גרעינית) ו NQR ומטרתן להוות דוגמאות פשוטות ומובנות יותר עליהן מסתמך פרק 4. ראיות ניסיוניות לכך שהטכניקה אכן ניתנת לביצוע מעשי, ומדידות התואמות לתאוריה מופיעות בפרק 2.
הרובד השני הוא שימוש מעשי בטכניקה למחקר פיסיקלי עכשוי, קרי, ניסיון להוסיף מידע לשאלה שהוצגה לעיל. יישמנו את הטכניקה הנ"ל עבור על מוליך בטמפ' גבוהה (YBCO), ואכן קיבלנו תוצאות חדשות המוסיפות להבנת הבעיה. תוצאות אלו, והמסקנות הנובעות מהן מפורטות בפרקים 2 ו 3. פרקים 5-7 מתארים את החלק הניסיוני של העבודה: תאור מבנה החומר, הכנת הדגמים ואיפיונם והאנליזה של הנתונים.
גם המסקנות המתקבלות מעבודה זאת ניתנות לחלוקה לשני רובדים אלו. אין כל ספק שהטכניקה אכן ישימה ותוצאותיה תואמות את הצפי התאורטי. מנגד, תהליך אנליזת הנתונים מצביע על כך שקיימים גורמים נוספים, שאת חלקם ציינו, שלא נלקחו בחשבון במהלך החישובים ומצריכים עבודה נוספת בתחום זה.
ברובד הניסיוני התוצאה העיקרית של העבודה היא שיש קורלאציה הפוכה בין אי-הומוגניות לעל מוליכות. כלומר ככל שהאי הומוגניות גדלה העל מוליכות דווקא נחלשת (בניגוד לתאורית הפסים).